Thesis for the Degree of Doctor of Philosophy

Evaluation of Hydrogen-Assisted Cracking Behavior of HV670 Steel using Elastic Wave, and Fatigue Life

by

Ki-Sik Lee

Department of Materials Science and Engineering

The Graduate School

Pukyong National University

February 2023

Evaluation of Hydrogen-Assisted Cracking Behavior of HV670 Steel using Elastic Wave, and Fatigue Life

Advisor: Prof. Ki-Woo Nam

by

Ki-Sik Lee

A thesis submitted in partial fulfillment of the requirements

for the degree of

Doctor of Philosophy

in Department of Materials Science and Engineering, The Graduate School,

Pukyong National University

February 2023

Evaluation of Hydrogen-Assisted Cracking Behavior of HV670 Steel using Elastic Wave, and Fatigue Life

A Dissertation

by

Ki-Sik Lee

Approved by February 17 2023

An, Byung-Gun

(Chairman)

Kang, Heoung-Joo

(Member)

Kim, Kong-Young

(Member)

Hyun, Jae-Yong

(Member)

Nam, Hyungseok

(Member)

Content

Evaluation of Hydrogen-Assisted Cracking Behavior of HV670 Steel using Elastic Wave, and Fatigue Life

Ki-Sik Lee

Department of Materials Science and Engineering

The Graduate School

Pukyong National University

Abstract

The elastic waves generated in ultra-high strength steel (UHSS) under various corrosive solutions were investigated. The threshold stress intensity factor (K_{IHAC}) for HAC was obtained from ultra-high strength steel (SKD11: HV670) by applying different loads in a solution of 0.057M acetic acid. The frequency characteristics by hydrogen aggregation and crack propagation were analyzed by the time-frequency analysis method using LabVIEW. The K_{IHAC} of the specimen was determined from the cumulative elastic wave and fracture surface, and the static fatigue limit based on the crack depth was determined using K_{IHAC}. Regardless of the corrosion solution, elastic waves in a low frequency band, less than 40 kHz, and in a high frequency band, more than 60 kHz, were obtained. The low frequency below 40 kHz was caused by corrosion, while the high frequency above 60 kHz are caused by crack initiation and propagation. The elastic wave in the specimens under the acetic acid solution were caused by HAC-induced crack propagation, but the elastic wave in the specimens under 1.5M H_2SO4 + NaCl 0.5M solution or distilled water were strongly affected by corrosion. The frequency band of the elastic wave was divided into dominant frequency below about 50 kHz and above about 60 kHz, regardless of the value of Kc. The low-frequency band below about 50 kHz is the elastic wave due to corrosion, while the high-frequency band above about 60 kHz is

the elastic wave caused by crack occurrence and propagation. When K_C was the smallest, the crack in the surface direction propagated slightly, but the crack in the depth direction did not propagate at all. The stress intensity factor at this time was determined as the HAC threshold stress intensity factor (K_{IHAC}). That is, K_{IHAC} was determined to be 1.96 MPa$\sqrt{m}$. The static fatigue limit was determined to be 400 MPa, and the static fatigue limit of the crack specimen can be evaluated using $K_{IHAC(a)}$ = 1.96 MPa$\sqrt{m}$). The experimental results agreed well with the evaluation results.

Chapter 1

Introduction

In general, when steel fractures in a hydrogen atmosphere or a hydrogen-generating atmosphere, it exhibits three fracture modes [1-5]: micro-void coalescence (MVC), quasi-cleavage (QC), and inter-granular (IG) fracture modes depending on the conditions. In the case of steel with high yield strength, the propagation probability in IG mode is high, whereas the proportion of QC mode or MVC mode in the fracture surface increases as the yield strength decreases [3,4]. Among the fracture surface, since the fracture energy of IG mode is the lowest, high-strength steel is more sensitive to hydrogen-assisted cracking. Therefore, the study of hydrogen-assisted cracking is most important for structural maintenance.

Griffith [6] was the first to propose an energetic criterion for the energy change associated with crack propagation. This criterion played a very important role in establishing and developing the concept of fracture mechanics. In particular, it has been widely used because it is very convenient to consider thermodynamic quantities and can be applied regardless of which process the crack propagation was governing.

There are many studies of hydrogen-assisted cracking (HAC) on the dependence of K_{th} on hydrogen concentration or hydrogen fugacity [7-13]. However, there are few studies related to elastic waves [14,15]. The fugacity of a real gas, in chemical thermodynamics, is an effective partial pressure which replaces the mechanical partial pressure in an accurate computation of the chemical equilibrium constant. It is equal to the pressure of an ideal gas which has the same temperature and molar Gibbs free energy as the real gas.

In the first study, elastic waves generated from ultra-high-strength steel (HV670) with different corrosion solutions were detected, and frequency characteristics were analyzed using time-frequency analysis using LabVIEW. In the second study, the threshold stress intensity factor (K_{IHAC}) for HAC of HV670 steel was obtained by applying different loads in the solution of 0.057M acetic acid. In addition, the elastic wave was detected from the crack and analyzed the frequency characteristics due to hydrogen aggregation and crack propagation by time-frequency analysis using LabVIEW. The crack propagation was

observed from the cumulative elastic wave and the fracture surface, and the K_{IHAC} was determined. The third study evaluated the threshold stress intensity factor and static fatigue limit of HV670 steel in a corrosive environment to prevent structural damage due to HAC. In addition, elastic waves generated from the crack were detected, and frequency characteristics due to hydrogen aggregation and crack propagation were analyzed using time-frequency analysis using LabVIEW. K_{IHAC} of the hydrogen-assisted stress corrosion cracking was determined from the cumulative elastic wave and the fracture surface, and the static fatigue limit according to the crack depth was determined from K_{IHAC}.

References

1. I. M. Bernstein, 1970, “Hydrogen-induced cracking in iron: Morphology and crack path dependence“, Metallurgical Transactions, Vol. 1, pp. 3143-3150.
2. C. D. Beachem, 1972, “A new model for hydrogen-assisted cracking (hydrogen “embrittlement”)“, Metallurgical and Materials Transactions B, Vol. 3, pp. 441-455.
3. G. Sandoz, 1972, “A Unified Theory for Some Effects of Hydrogen Source, Alloying Elements, and Potential on Crack Growth in Martensitic AISI 4340 Steel”, Metallurgical Transactions, Vol. 3, pp. 1972-1169.
4. M. Watkins, M. F. Bluem, J. B. Greer, 1976, “Fractography of sulfide stress cracking”, Corrosion, Vol. 32, pp. 102-109.
5. M. Gao, R. P. Wei, 1985, “A "Hydrogen Partitioning" Model for Hydrogen Assisted Crack Growth”, Metallurgical Transactions, Vol. 1,6A pp. 1985-2039.
6. A. A. Griffith, 1921, “The Phenomena of Rupture and Flow in Solids”, Philosophical Transactions of the Royal Society of London, Series A, Vol. 221, pp. 163-198.
7. R. A. Oriani, P. H. Josephic, 1974, “Equilibrium aspects of hydrogen-induced cracking of steels”, Acta Metallurgical, Vol. 22, pp. 1065-1074.
8. W. W. Gerberich, Y. T. Chen, and C. St. John, 1975, “A short-time diffusion correlation for hydrogen-induced crack growth kinetics”, Metallurgical Transactions, Vol. A6, pp. 1485-1498.
9. P. Doig, G. T. Jones, 1977, “A model for the initiation of hydrogen embrittlement cracking at notches in gaseous hydrogen environments”, Metallurgical and Materials Transactions A, Vol. 8, pp. 1993-1998.
10. R. Thomson, 1978, “Brittle fracture in a ductile material with application to hydrogen embrittlement”, Journal of Materials Science, Vol. 13, pp. 128-142.
11. K. N. Akhurst, T. J. Baker, 1981, “The threshold stress intensity for hydrogen-induced carck growth,” Metallurgical Transactions A, Vol. 12, pp. 1059-1070.
12. S. V. Nair, R. R. Jensen, J. K. Tien, 1983, “Kinetic enrichment of hydrogen at interfaces and voids by dislocation sweep-in of hydrogen”, Metallurgical Transactions A, Vol. 14, pp. 385-393.
13. J. Kameda, 1986, “A microscopic model of hydrogen-induced intergranular cracking—I. Equilibrium crack growth“, Acta Metallurgical, Vol. 34, pp. 867-882.

14. Y. Hayashi, T. Terasawa, M. Takemoto, 1991, “Microkinetics of Hydrogen Assisted Cracking by Inversion Processing of Elastic Waves Utilizing Theoretical Green's Function”, Zairyo-to-Kankyo, Vol. 40, pp. 478-486.
15. K. S. Lee, J. E. Paeng, K. H. Gu, K. W. Nam, 2021, “Threshold stress intensity factor of ultra-high strength steel (HV670) containing surface crack by hydrogen assisted cracking and cumulative elastic wave”, Journal of Mechanical Science and Technology, Vol. 35, pp. 2441–2447

Chapter 2

Elastic Wave Properties in Ultra-High Strength Steel (HV670) exposed to Various Corrosive Solutions

2.1 Introduction

Due to its excellent resistance to fatigue, high strength, high toughness ultra-high-strength steel is often chosen for use in the landing gears and fasteners of aircraft. For such components, if ultra-high-strength steel is used, the final product becomes lighter and the manufacturing cost can be reduced. However, these steels can experience severe hydrogen embrittlement after exposure to a corrosive environment [1]. Also, the components that use ultra-high-strength steels are constantly being stressed [2]. In hydrogen environments, if a steel component experiences stress that is higher than a certain critical value, hydrogen-assisted delayed fractures occur [3]. Hydrogen-assisted delayed fractures are one of the most serious threats to safety faced by the aerospace industry. Motivated by this, hydrogen-assisted cracking (HAC) of high-strength steel has been widely studied in various environments [4-16]. This study mainly focuses on qualitative hydrogen embrittlement, however, a quantitative study was also conducted [12-14]. In order to secure the safety of a structure at risk from hydrogen-assisted cracking, there have been some studies that analyzed how elastic waves in steel are affected by the initiation and propagation of cracks [15,16]. However, there are no studies that have attempted to detect and analyze elastic waves generated in steel while exposed to various solutions.

In this chapter, the elastic waves generated in ultra-high-strength steel (UHSS) under various corrosive solutions were investigated, we paid particular attention to the frequency characteristics of the waves by conducting a time-frequency analysis using LabVIEW. The results from this analysis provide the basic data for monitoring crack initiation and propagation in UHSS structural components that have been exposed to various harsh environments.

2.2 Materials and experimental method

The particular material investigated in this study was SKD11 cold-work mold steel, which was heat-treated to obtain UHSS. During heat treatment, the steel was kept at 1,036°C for 2 hours and quenched, then tempered at 180°C for 3 hours. The Vickers hardness (HV) of the UHSS obtained after the heat treatment was 670. The chemical compositions of SKD11 are shown in Table 2.1.

Fig. 2.1 shows the specimen used in this experiment. The slit in the specimen was machined in the center of a width of 10 mm by electric discharge machining (EDM). The semi-circle slit in the specimen used has $2c$=1.4 mm and a=0.7 mm, the crack aspect ratio is a/c=1. The applied stresses at the free end of the specimen were 98 MPa, 104 MPa, and 138 MPa. During testing, three types of solution were used: H_2SO_4 1.5M + NaCl 0.5M, distilled water, and 0.057M acetic acid.

Table 2.1 Chemical Compositions of SKD11 used in this study.

C	Si	Mn	P	S	Ni	Cr	Mo	V
1.489	0.272	0.329	0.024	0.001	0.239	11.29	0.843	0.236

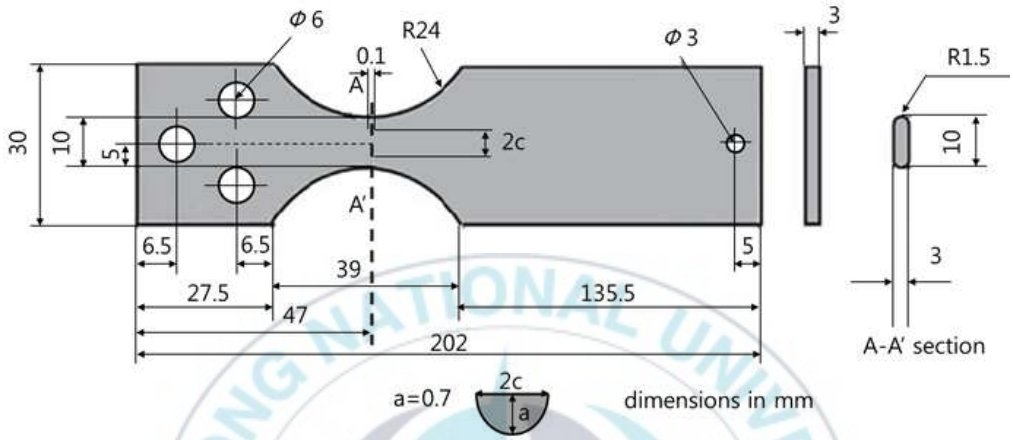

Fig. 2.1 SKD11 specimen used in this experiment.

The acquisition equipment used to record the elastic wave signals was the NI PXIe SYSTEM which supports up to 8 channels. The equipment digitizes and saves all elastic waves detected. The sampling rate used was 1MHz with a sampling size of 4,096. The sensor used 1MHz broadband with a wide frequency response range, the detected signals were passed through a 28dB preamplifier.

The sensor was fixed to the specimen with the contact medium. Fig. 2.2 shows the experimental apparatus used for elastic wave acquisition. The elastic wave signals were analyzed for their time-frequency using LabVIEW. After the experiment, a cross-section of the specimen was observed using SEM.

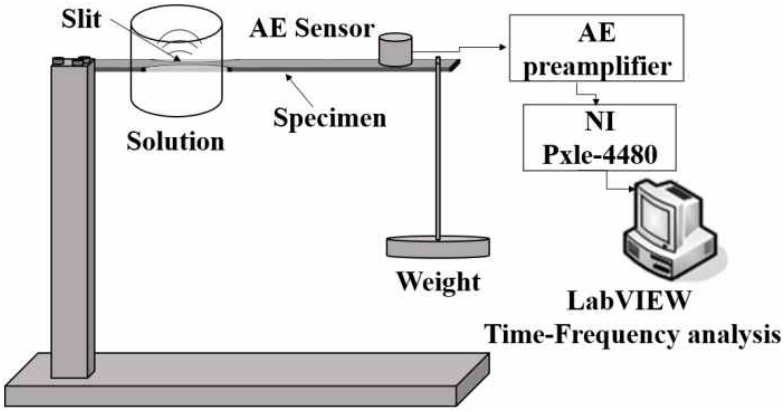

Fig. 2.2 Experimental apparatus for elastic wave acquisition.

2.3 Results and Discussion

2.3.1 Frequency band under corrosive solution

Fig. 2.3 shows the results of the waveform, frequency spectrum, and time-frequency analysis obtained under a corrosive solution of 1.5M H_2SO_4 + 0.5M NaCl. The results were obtained while under the corrosive solution but without any applied stress. The frequency band of the detected was is approximately 30 kHz.

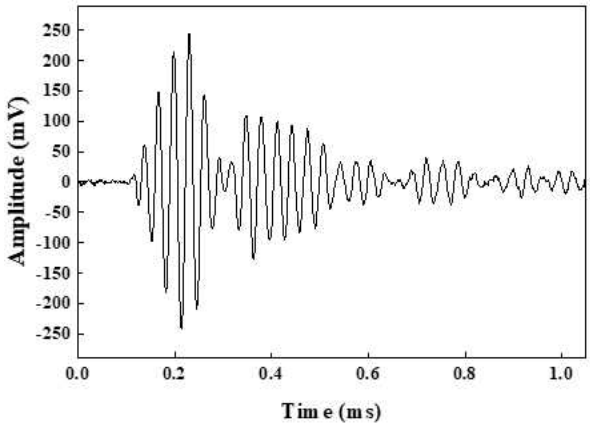

(a)

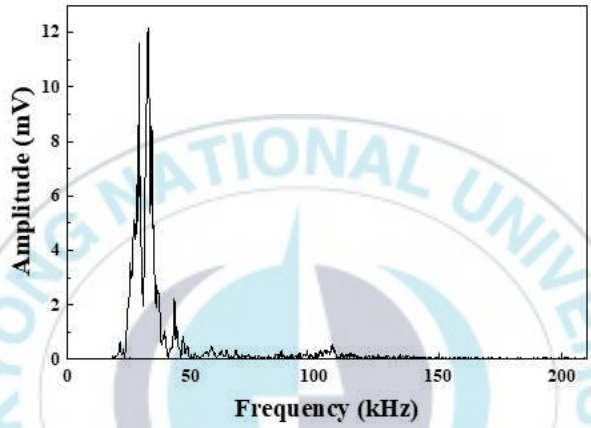

(b)

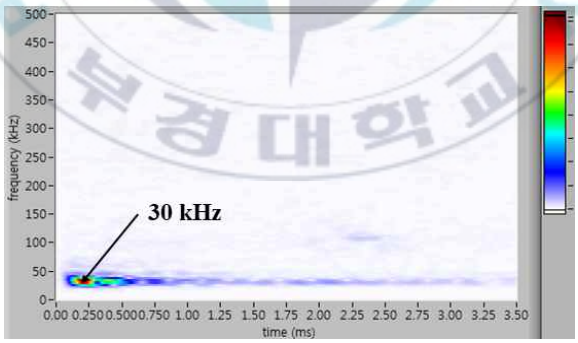

(c)

Fig. 2.3 Elastic wave signal obtained under a corrosive solution of 1.5M H_2SO_4 + 0.5M NaCl (no stress applied, only a corrosive environment).

2.3.2 Frequency band under a corrosive solution of 1.5M H_2SO_4 + 0.5M NaCl

Figs. 2.4 and 2.5 show the waveform, frequency spectrum, and time-frequency analysis obtained under a corrosive solution of 1.5M H_2SO_4 + 0.5M NaCl. These results were obtained while tensile stress of 13.5% was applied. Figs. 2.4 and 2.5 show the results obtained after 20 and 27 hours, respectively. In these figures, (a) shows the waveform, (b) shows the power spectrum, and (c) shows the time-frequency analysis.

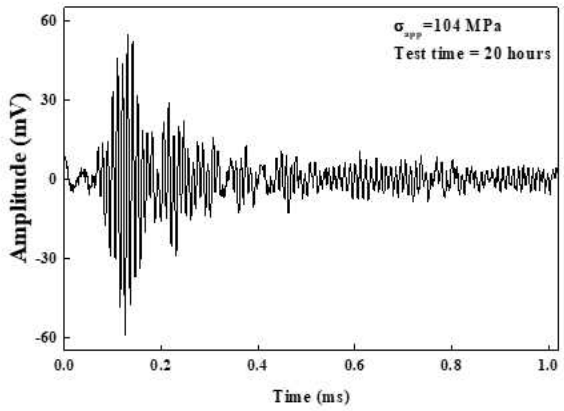

(a)

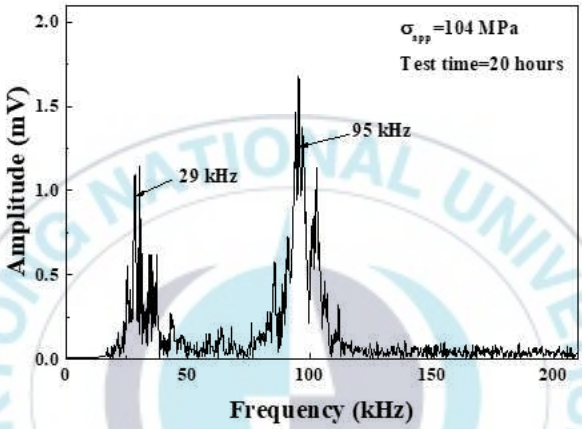

(b)

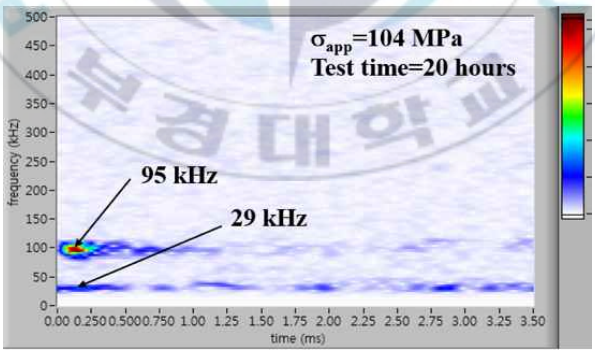

(c)

Fig. 2.4 Elastic wave signal obtained after 20 hours under a corrosive solution of 1.5M H_2SO_4 + 0.5M NaCl.

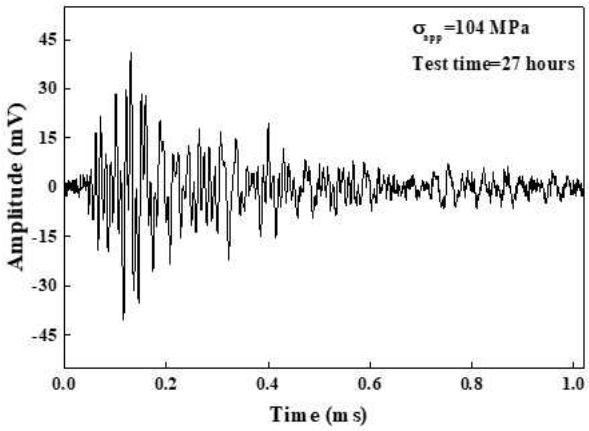

(a)

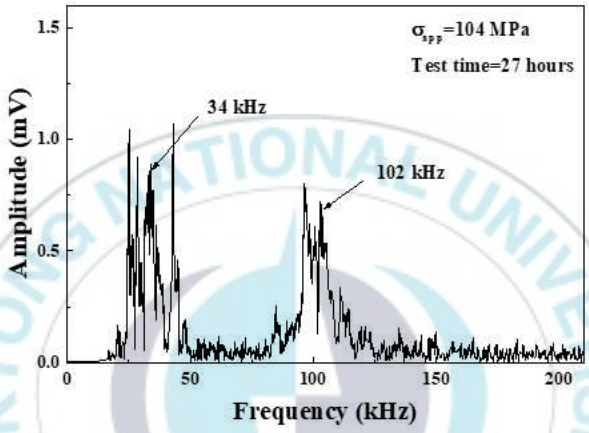

(b)

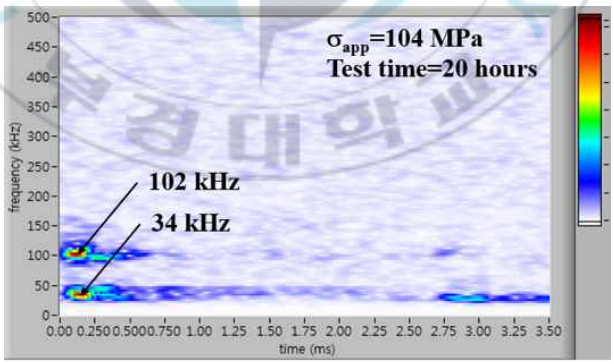

(c)

Fig. 2.5 Elastic wave signal obtained after 27 hours under a corrosive solution of 1.5M H_2SO_4 + 0.5M NaCl.

Fig. 2.6 shows the cumulative count and the dominant frequency of the elastic waves obtained from steel specimen while under a corrosive solution of 1.5M H_2SO_4 + 0.5M NaCl. The dominant frequencies were obtained from Figs. 2.4 and 2.5. Elastic waves were not seen until 19 hours into the experiment. This period is thought to be the time it takes for hydrogen aggregation to occur at the crack tip. The elastic waves accumulated rapidly and continuously from 19 to 32 hours. In this period, a lot of low-frequency band f(1) waves were recorded, but high-frequency band f(2) waves were not continuously present but just appeared from time to time. From 32 hours to the end of the experiment, we were still seeing occasional waves in the f(1) band, but none were seen in the f(2) band during the same period. We believe that no f(2) signals were obtained because the crack tip had become covered with a corrosive film due to excessive corrosion. A lot of low-frequency band f(1) waves between roughly 29 to 32 kHz were obtained due to corrosion, and high-frequency band f(2) waves around 95 kHz were obtained around 19 hours into the experiment. In addition, a lot of high-frequency band f(2) waves from 104 to 136kHz were obtained after 25 hours.

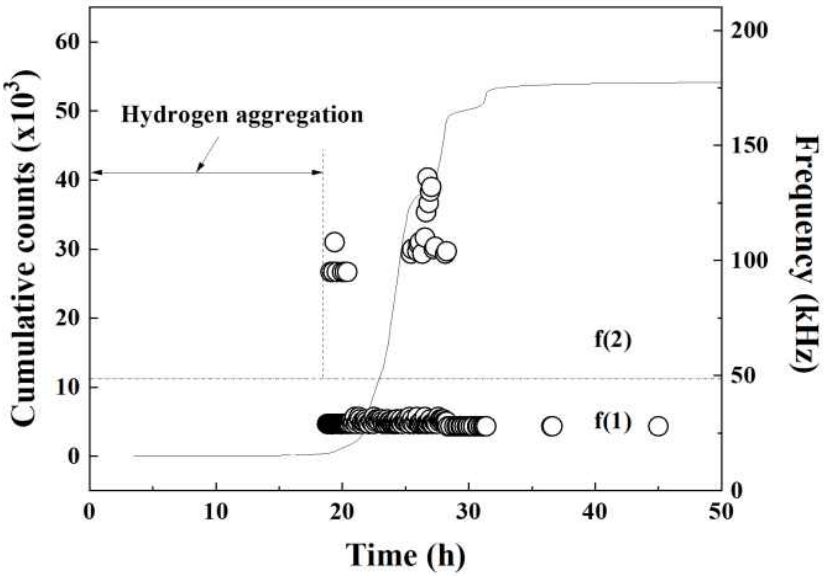

Fig. 2.6 Relationship between cumulative count, dominant frequency, and test time under a corrosive solution of 1.5M H_2SO_4 + 0.5M NaCl.

Fig. 2.7 shows SEM photographs of the fracture surface from the experiment using the corrosive solution of 1.5M H_2SO_4 + 0.5M NaCl. (a) shows the portion of the slit created by electrical discharge machining and the specimen surface. It can be seen that the surface is bumpy due to corrosion caused by the strong acid. (b) shows a portion of the slit after being exposed to strong acid, here we can see the presence of dents and corrosion. (c) shows a portion of the slit tip, we believe that the cracks were seen here propagated due to the corrosion and applied stress. The frequency band f(1) around 30 kHz is the dominant frequency for elastic waves occurring due to corrosion, the frequency band f(2) around 50 kHz or more is thought to be the dominant frequency related to crack initiation and propagation.

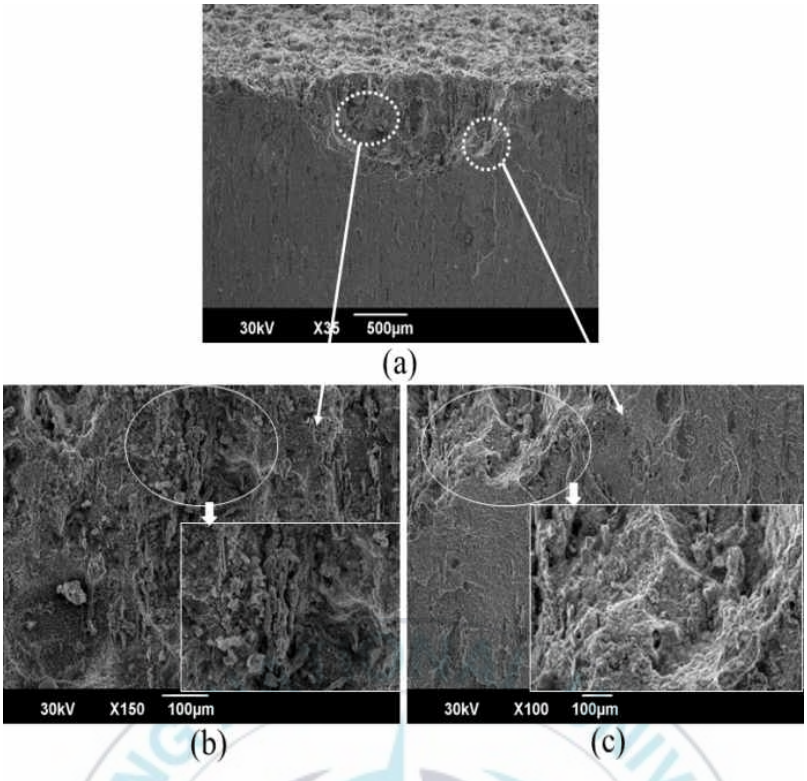

Fig. 2.7 SEM photograph of specimen under a corrosive solution of 1.5M H_2SO_4 + 0.5M NaCl. (a) Portion of slit created by EDM and specimen surface, (b) Portion of the corroded slit, (c) Portion of the slit tip.

2.3.3 Frequency band under distilled water

Figs. 2.8 and 2.9 show the results of the waveform, frequency spectrum, and time-frequency analysis obtained from specimen under distilled water while the tensile stress of 18% was applied. Figs. 2.8 and 2.9 show the elastic wave signal obtained after 23 and 61 hours, respectively. In these figures, (a) shows the waveform, (b) shows the power spectrum, and (c) shows the time-frequency analysis.

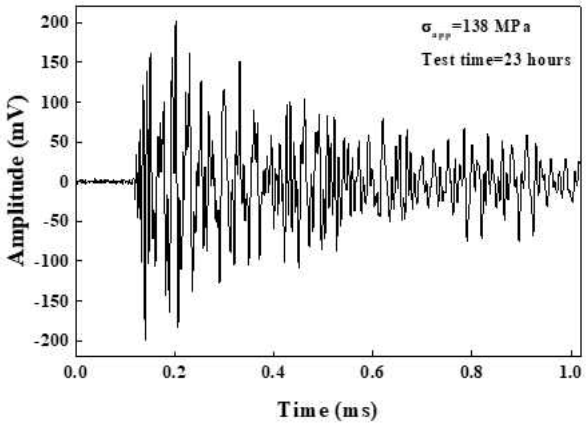

(a)

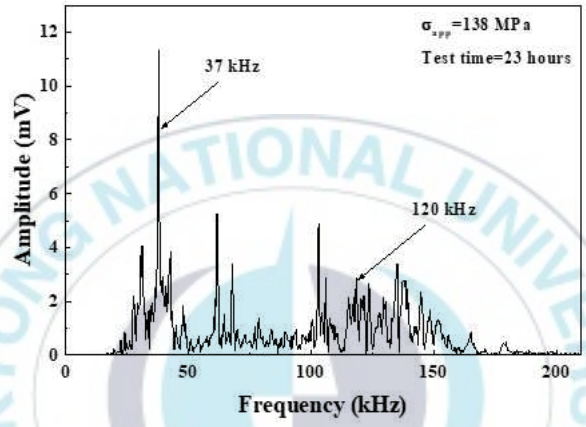

(b)

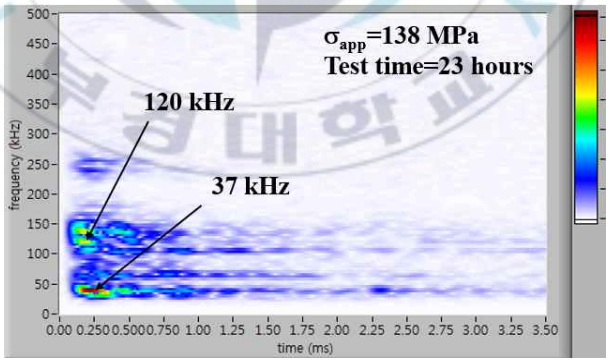

(c)

Fig. 2.8 Elastic wave signal obtained after 23 hours from specimen under distilled water.

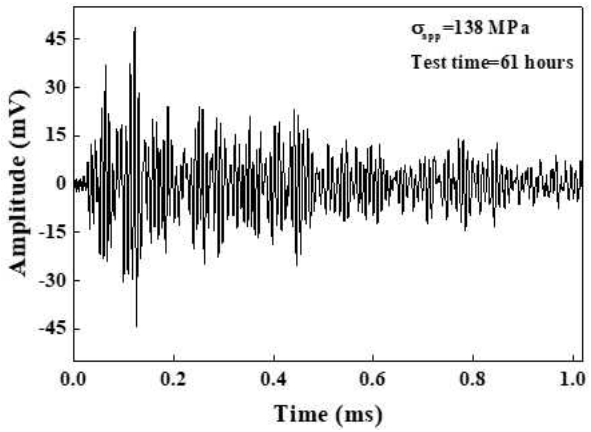

(a)

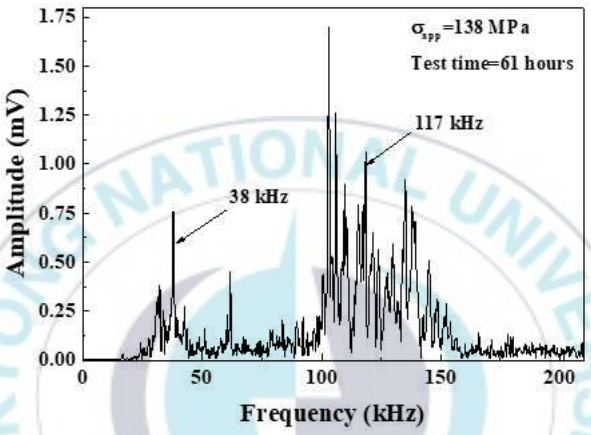

(b)

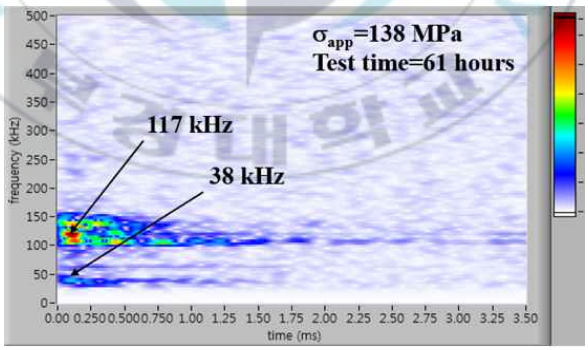

(c)

Fig. 2.9 Elastic wave signal obtained after 61 hours from specimen under distilled water.

Fig. 2.10 shows the cumulative count and dominant frequency of the elastic waves obtained from specimen under distilled water according to test time. No elastic waves were detected from roughly 19 to 22 hours, 26 to 40 hours, and 46 to 61 hours. It is thought that this in this period corrosion products and hydrogen aggregation at the slit tip were occurring. Elastic wave signals were obtained in the periods from 0-19 hours, 22-26 hours, and 40-46 hours as well as at about 61 hours. It is considered that this period fractured the corrosion products due to hydrogen aggregation and stress concentration at the slit tip, and cracks initiated and was propagated. From 61 hours to the end of the experiment, none were seen elastic wave signal. In distilled water, the dominant frequency of the elastic waves was obtained either in the low-frequency band f(1) from about 34 to 39 kHz or in the high-frequency band f(2) from about 91 to 149 kHz.

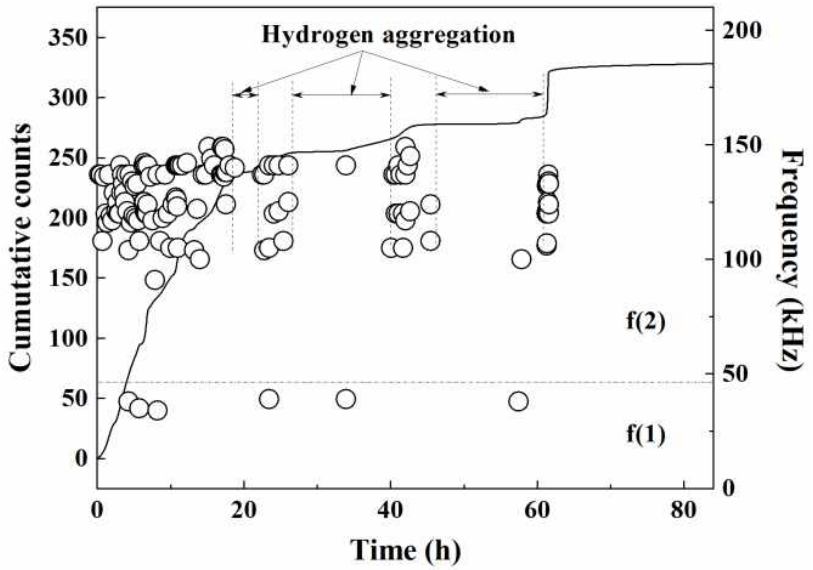

Fig. 2.10 Relationship between cumulative count, dominant frequency, and test time under distilled water.

Fig. 2.11 is an SEM photograph of the fracture surface from the experiment with distilled water. (a) shows a portion of the slit created by electric discharge machining, (b) shows a portion of the corroded slit, and (c) and (d) shows the slit tip. In (b), we can see pitting in several places due to corrosion by the distilled water. In (c), HAC can be seen in some places due to the distilled water and applied stress. In the enlarged figure, we can clearly see grains caused by the embrittlement of the interface, and cracks can be observed in the cross-section of some parts. In addition, a lot of corrosion can be observed in this portion of the slit. In (d), a lot of corrosion can also be seen in this portion of the slit, and it is considered that the crack shown here initiated at the slit tip. In distilled water, HAC occurred due to hydrogen aggregation, while the crack propagated due to the applied stress. It is thought that no elastic waves were detected after 61 hours due to the closure of the crack tip by corrosion.

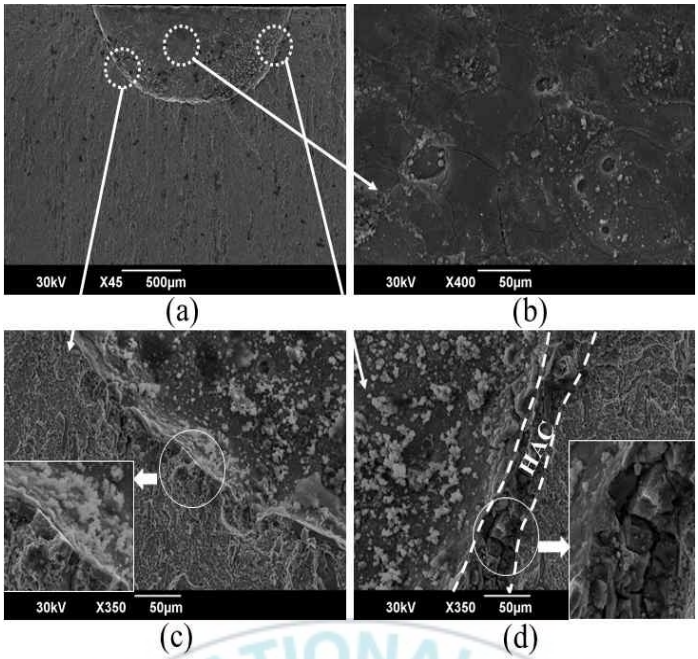

Fig. 2.11 SEM photographs of the specimen after experiment under distilled water. (a) Portion of slit created by EDM, (b) Portion of the corroded slit, (c), and (d) Portion of slit tip.

2.3.4 Frequency band under 0.057M acetic acid

Figs. 2.12 and 2.13 show the results of the waveform, frequency spectrum, and time-frequency analysis from the specimen under a solution of 0.057M acetic acid while the tensile stress of 12.4% was applied. Figs. 2.12 and 2.13 show the elastic wave signal obtained after 21 and 283 hours, respectively. In these figures, (a) shows the waveform, (b) shows the power spectrum, and (c) shows the time-frequency analysis.

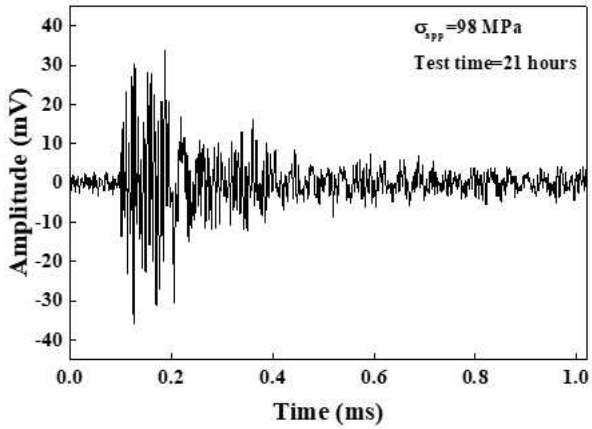

(a)

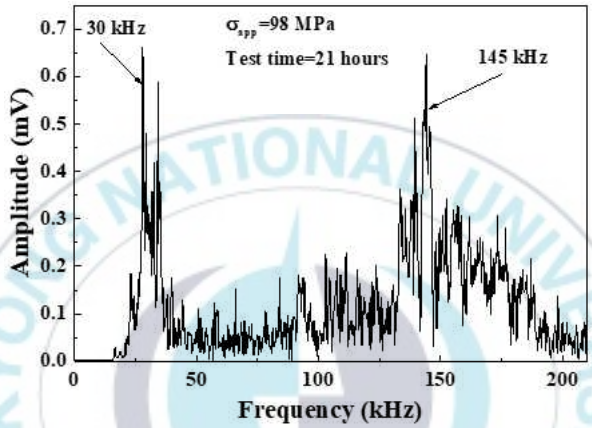

(b)

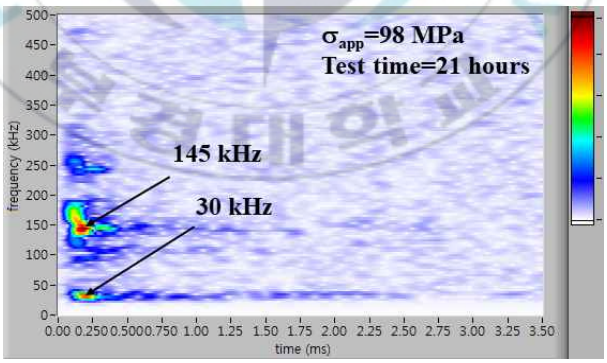

(c)

Fig. 2.12 Elastic wave signal obtained after 21 hours under a corrosive solution of 0.057M acetic acid.

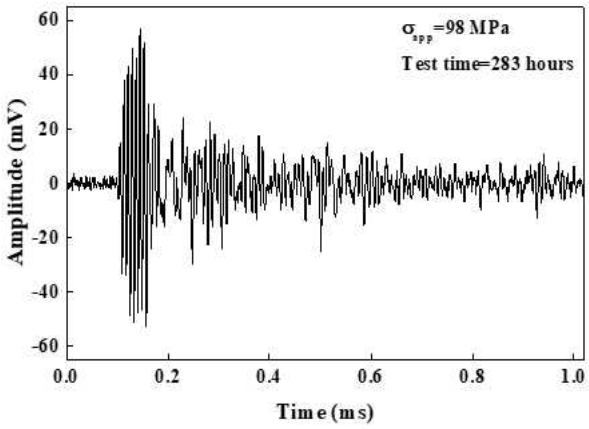

(a)

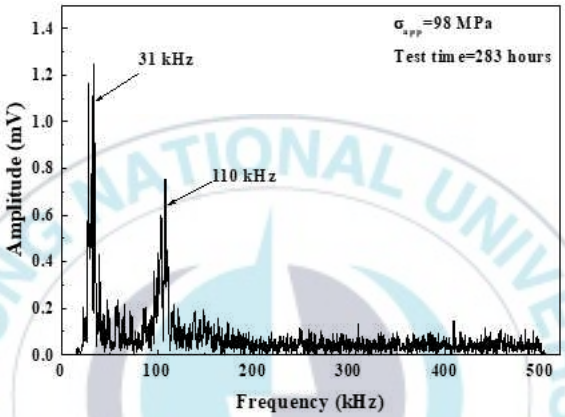

(b)

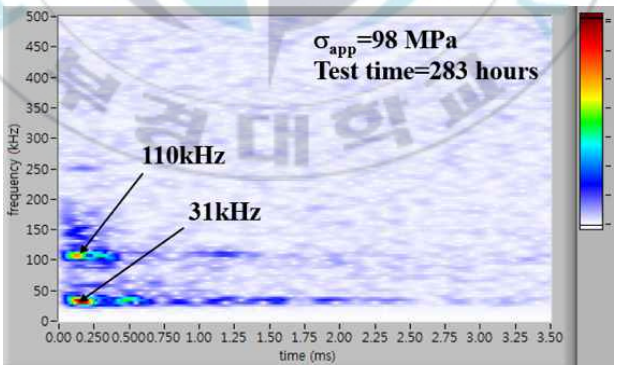

(c)

Fig. 2.13 Elastic wave signal obtained after 283 hours under a corrosive solution of 0.057M acetic acid.

Fig. 2.14 shows the cumulative count and dominant frequency of elastic waves obtained from specimens under 0.057M acetic acid according to test time. (a) shows the cumulative count and dominant frequency in steel specimen under a corrosive solution of 0.057M acetic acid according to test time up to about 500 hours, and (b) shows a magnification of the period from 0-282 hours. No elastic waves were detected in the periods from 0 to 18 hours, 63 to 137 hours, and 235 to 282 hours. During these periods it is considered that hydrogen aggregation was occurring at the slit tip. Elastic wave signals were obtained in periods from 18 to 63 hours, 137 to 235 hours, and from 282 hours to the end of the experiment. It is considered that during this period cracks had initiated due to hydrogen aggregation and were propagating. The dominant frequency of the elastic waves was either in the low-frequency band f(1) around 32-40 kHz or in the high-frequency band f(2) around 59-177 kHz. After 282 hours only waves in the low-frequency band f(1) around 32 kHz were detected, we believe these low-frequency elastic waves are the result of corrosion.

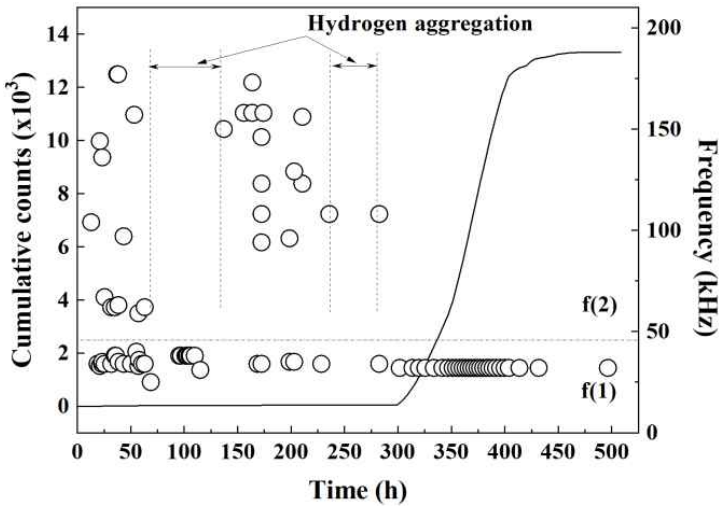

(a)

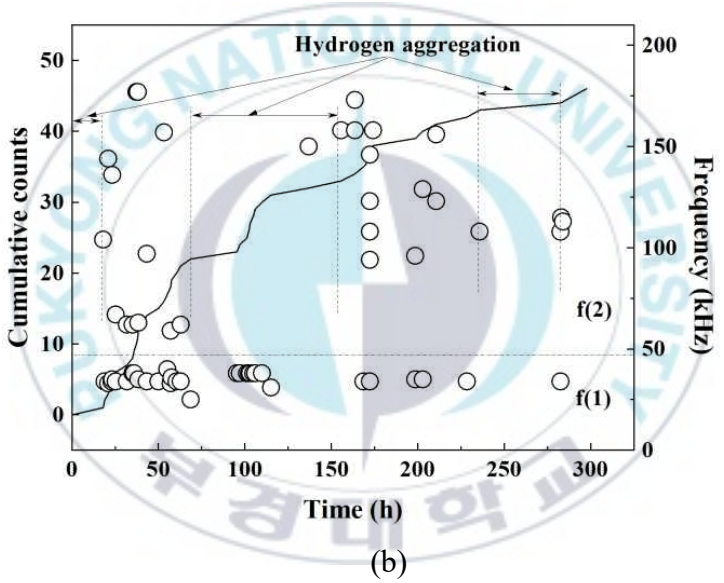

(b)

Fig. 2.14 (a) Relationship between cumulative count, dominant frequency, and test time under a corrosive solution of 0.057M acetic acid, (b) Magnification of 0～282 hours.

Fig. 2.15 shows SEM photographs of the fracture surface from the experiment with 0.057M acetic acid. (a) shows a portion of the slit created by electric discharge machining. (b) to (d) show the tip portion of the slit where hydrogen embrittlement crack initiates. It is believed that the crack that initiated at the slit tip propagated due to some corrosion and the applied stress. In the enlarged figure of (b)-(d), we can see the interface of the HAC portion was embrittled and the grains can be clearly observed, we can see a crack in some part of the cross-section. Elastic waves in the frequency band below about 40 kHz were caused by corrosion, while elastic waves in the frequency band above about 60 kHz are judged to be caused by crack initiation and propagation.

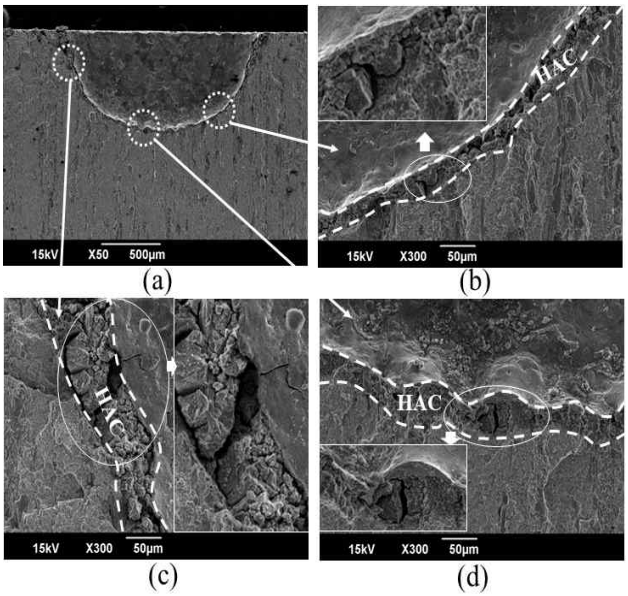

Fig. 2.15 SEM photograph under a corrosive solution of 0.057M acetic acid. (a) Portion of slit created by EDM, (b)～(d) Slit tip

2.4 Summary

In this chapter, elastic waves in an SKD11 (HV670) specimen under three types of corrosive solution were investigated, in particular, the frequency characteristics of these elastic waves were studied by time-frequency analysis using LabVIEW.

1) Regardless of the corrosion solution, elastic waves in a low-frequency band, less than 40 kHz, and elastic waves in a high-frequency band, more than 60 kHz, were obtained.
2) The low frequency below 40 kHz is caused by corrosion, while the high frequency above 60 kHz is caused by crack initiation and propagation.
3) The causes of elastic wave signal were differed according to the corrosive solution used. Generally, the elastic wave in the specimens under the acetic acid solution was caused by HAC-induced crack propagation, but the elastic wave in the specimens under 1.5M H_2SO_4 + NaCl 0.5M solution or distilled water was strongly affected by corrosion.

References

1. M. R. Louthan Jr., G. R. Caskey Jr., J. A. Donovan and D. E. Rawl Jr., 1972, “Hydrogen embrittlement of metals”, Materials Science and Engineering, Vol. 10, pp. 357-368.
2. J. Toribio and M. Elices, 1991, “Influence of residual stresses on hydrogen embrittlement susceptibility of prestressing steels”, International Journal of Solids and Structures, Vol. 28, pp. 791-803.
3. W. Y. Chu, J. Yao and C. M. Hsiao, 1984, “Hydrogen Induced Slow Crack Growth in Stable Austenitic Stainless Steels”, Metallurgical Transactions A, Vol. 15, pp. 729–733.
4. D. Figueroa and M. J. Robinson, 2010, “Hydrogen transport and embrittlement in 300 M and AerMet100 ultra high strength steels”, Corros. Sci., Vol. 52, pp. 1593-1602.
5. L. W. Tsay, H. L. Lu and C. Chen, 2008, “The effect of grain size and aging on hydrogen embrittlement of a maraging steel”, Corros. Sci., Vol. 50, pp. 2506-2511.
6. B. G. Pound, 2000, “The effect of aging on hydrogen trapping in precipitation-hardened alloys”, Corros. Sci., Vol. 42, pp. 1941-1956.
7. D. Hardie, E.A. Charles and A.H. Lopez, 2006, “Hydrogen embrittlement of high strength pipeline steels”, Corros. Sci., Vol. 48, pp. 4378-4385
8. D. Figueroa and M. J. Robinson, 2008, “The effects of sacrificial coatings on hydrogen embrittlement and re-embrittlement of ultra-high-strength steels”, Corros. Sci., Vol. 50, pp. 1066-1079.
9. L. W. Tsay, M. Y. Chi, Y. F. Wu, J. K. Wu and D. Y. Lin, 2006, “Hydrogen embrittlement susceptibility and permeability of two ultra-high-strength steels”, Corros. Sci., Vol. 48, pp. 1926-1938.
10. W. Y. Chu, T. H. Liu, C. M. Hsiao and S. Q. Li, 1981, “Mechanism of stress corrosion cracking of low alloy steel in water”, Corrosion, Vol. 37, pp. 320-327.
11. L. W. Tsay, Y. F. Hu, C. Chen, 2005, “Embrittlement of T-200 maraging steel in a hydrogen sulfide solution”, Corros. Sci., Vol. 47, pp. 965-976.
12. W. Y. Chu, L. J. Qiao, Y. B. Wang and Y. H. Cheng, 1999, “Quantitative study for sulfide stress corrosion cracking of tubular steel”, Corrosion, Vol. 55, pp. 667-673.
13. H. L. Li, K. W. Gao, L. J. Qiao, Y. B. Wang and W. Y. Chu, 2001, “Strength effect in stress corrosion cracking of high-strength steel in aqueous solution”, Corrosion,

Vol. 57, pp. 295-299.

14. Y. P. Zhang, D. M. Shi, W. Y. Chu, L. J. Qiao, Y. L. Shi, S. L. Zheng and S. B. Wang, 2007, “Hydrogen-assisted cracking of T-250 maraging steel“, Mater. Sci. Eng. A, Vol. 471, pp. 34-37.
15. D. D. Dedhia and W. E. Wood, 1981, ”Application of acoustic emission analysis to hydrogen-assisted cracking“, Materials Science and Engineering, Vol. 49, pp. 263-273.
16. A. K. Bhattacharya, N. Parida and P. C. Gope, 1992, “Monitoring hydrogen embrittlement cracking using acoustic emission technique”, Journal of Materials Science, Vol. 27, pp. 1421–1427.

Chapter 3

Threshold Stress Intensity Factor of Ultra-High Strength Steel (HV670) containing Surface Crack by Hydrogen-Assisted Cracking and Cumulative Elastic Wave

3.1 Introduction

Metal components, such as power plants, offshore structures, and the pressure vessels or pipes of hydrogen vehicles, when exposed to active hydrogen atmosphere during service, show hydrogen embrittlement that degrades mechanical properties [1-5]. When the structure is exposed to a hydrogen atmosphere or an acidic substance, and a mechanical load is applied, the risk of failure may increase, due to hydrogen intrusion into and interaction with the microstructure. Hydrogen-assisted cracking (HAC) due to hydrogen embrittlement is likely to occur in ultra-high-strength steel (UHSS) [6-15]. HAC is not observed below the threshold stress intensity factor (K_{th}) [15] and shows the crack growth rate da/dt at a stress intensity factor (K) above K_{th}.

Hydrogen damage is caused by the reduction of bond strength or interactions of hydrogen plasticity [6,7,16-20]. K_{th} and Stage II are affected by the steel sensitivity and many parameters [6,15,21]. The parameters are the microstructure characteristics, hydrostatic stress of the crack tip, and the amount of hydrogen accumulated in the process zone [7,15]. As yield strength increases for hydrogen concentration, K_{th} decreases, and Stage II rate increases [12,15]. High-strength steel AISI 4340 is susceptible to intergranular HAC. The separation of impurities at the grain boundary results in them interacting with hydrogen and decreases the cohesion at the boundary. Therefore, K_{th} is much lower than the plane strain fracture toughness K_{IC} without hydrogen [7,8,10,12].

After the theory of HAC was introduced by Zapfe and Sims in the 40s, various mechanisms and theories have been proposed to explain the microstructure of metal structures under mechanical load and the hydrogen concentration of specific metals [22-26]. Li et al were examined elastic wave activity increased during hydrogen charging using low-carbon steel [27]. Bae et al were used to evaluate the dynamic behavior of the

hydrogen charged austenitic stainless steel specimen using the acoustic emission (AE) technique [28]. However, it is necessary to study the elastic wave characteristics and threshold stress intensity factors according to crack occurrence and propagation in the HAC atmosphere.

This chapter obtained the threshold stress intensity factor (K_{IHAC}) for HAC in ultra-high-strength steel (SKD11: HV670) by applying different loads in a solution of 0.057M acetic acid. Elastic wave from the crack propagation of the specimen was detected, and the frequency characteristics by hydrogen aggregation and crack propagation were analyzed by the time-frequency analysis method using LabVIEW. The crack propagation of the specimen was observed from the cumulative elastic wave and the fracture surface, and K_{IHAC} was determined. These results will provide basic data for monitoring structures in which HAC occurs, and for predicting the HAC behavior of UHSS.

3.2 Material and Experiment Method

The material used in this study was SKD11 for cold mold steel, which was heat-treated to obtain UHSS for the HAC experiments. The heat-treatment conditions were quenching at 1,036 °C for 2h and tempering at 180 °C. The Vickers hardness (HV) of UHSS obtained by heat treatment was 670. Table 3.1 shows the chemical composition and the mechanical properties of SKD11. Fig. 3.1 shows the specimen with which the HAC experiment was carried out.

Table 3.1 Chemical compositions (wt.%) and mechanical properties of SKD11.

C	Si	Mn	P	S	Ni	Cr	Mo	V
1.489	0.272	0.329	0.024	0.001	0.239	11.29	0.843	0.236

σ_t (MPa)	σ_y (MPa)	E (GPa)
1158	1034	207

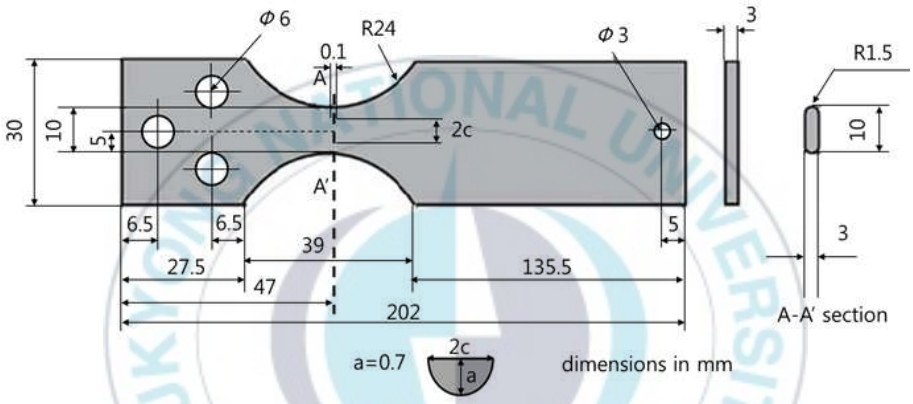

Fig. 3.1 Ultra-high-strength steel specimen for HAC.

The slit of the specimen was machined onto the center of a width of 10 mm by electric discharge machining (EDM). The semicircular slit of the specimen used in this study was $2c$=1.4 mm, a=0.7 mm, and the crack aspect ratio (a/c) was 1.0. The static stress loaded on the free end of the specimen was determined by the Newman–Raju equation [29] as following Eq. (3.1). That is, stress intensity factors (K_c and K_a) of the surface (c) and depth (a) of the slit were calculated. Acetic acid (0.057M) was used as the solution for the HAC experiment.

$$\mathrm{K} = (\sigma_t + H\sigma_b)\sqrt{\frac{\pi a}{Q}}\mathrm{F} \tag{3.1}$$

$$\mathrm{Q} = 1 + 1.464\left(\frac{a}{c}\right)^{1.65}$$

where σ_t is tension stress, σ_b is bending stress. The functions F and H are boundary-correction factors.

The NI PXIe SYSTEM, which supports up to 8 channels, was used to detect the waveform and frequency characteristics of the elastic wave signal. The equipment digitizes and saves all obtained elastic waves. The detection sampling rate of the elastic wave is 1MHz, and the sampling size is 4,096. The elastic wave detection sensor is a wideband sensor of 1MHz with a wide range of frequency response characteristics. The elastic wave was detected through a 28dB preamplifier. Time-frequency analysis of the detected elastic wave signal was carried out using LabVIEW. Fig. 3.2 shows a schematic of the experimental setup. The cross-section of the specimen was observed using SEM.

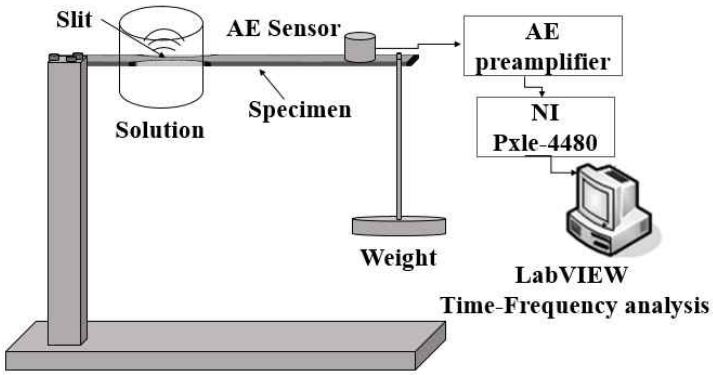

Fig. 3.2 Schematic of the experimental apparatus.

3.3 Results and discussion

3.3.1 Elastic wave obtained from the stress intensity factor K_c=8.11 M Pa$\sqrt{m}$ and K_a= 5.56 M Pa$\sqrt{m}$

Figs. 3.3 and 3.4 show the results of the waveform, frequency spectrum, and time-frequency analysis obtained when stresses, such as the stress intensity factor K_c=8.11 MPa$\sqrt{m}$ and K_a= 5.56 MPa$\sqrt{m}$, are applied to the surface crack. Figs. 3.3 and 3.4 show the results obtained at 27 and 430 hours, respectively. In each figure, (a) is the waveform, (b) is the power spectrum, and (c) is the time-frequency analysis.

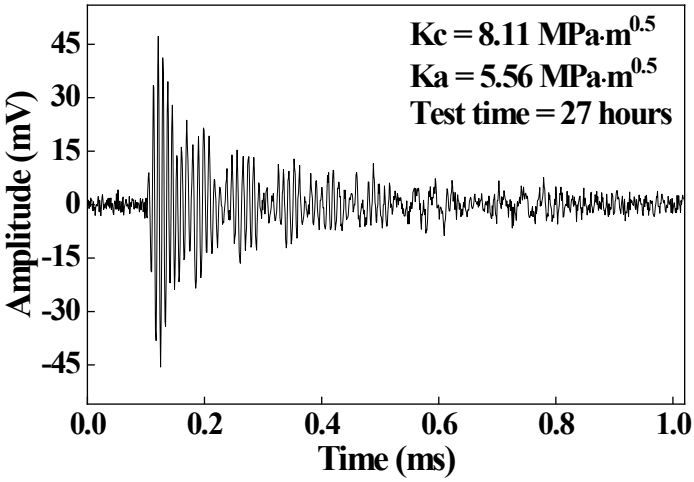

(a)

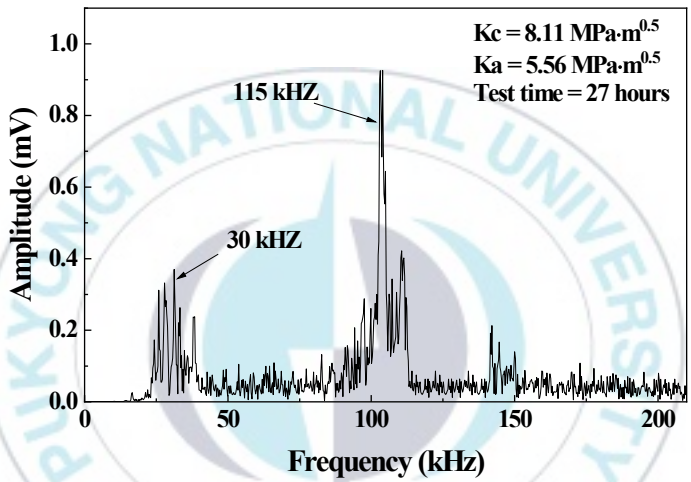

(b)

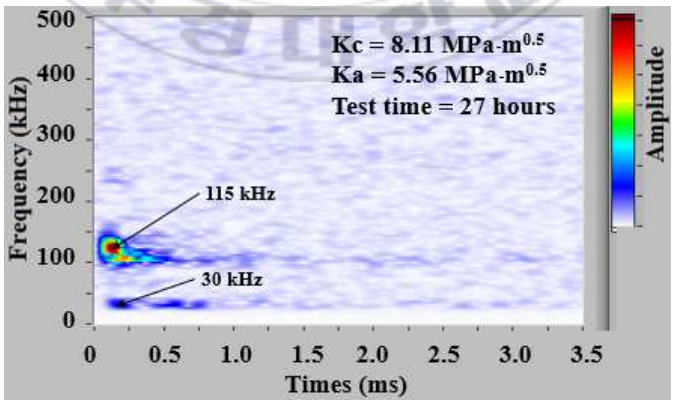

(c)

Fig. 3.3 Elastic wave signal obtained from 27 hours of $K_c = 8.11$ MPa$\sqrt{\text{m}}$ and $K_a = 5.56$ MPa$\sqrt{\text{m}}$. (a) Waveform, (b) Power spectrum, (c) Time-frequency analysis.

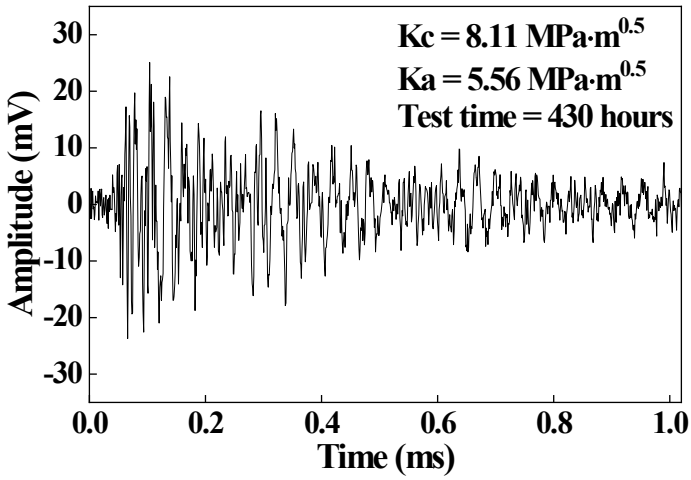

(a)

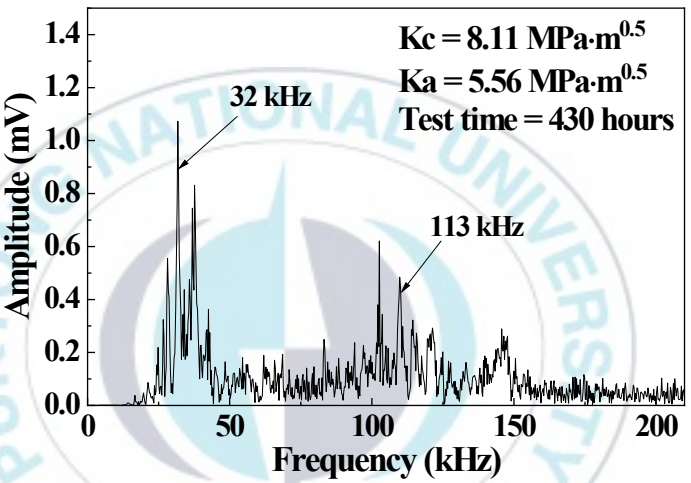

(b)

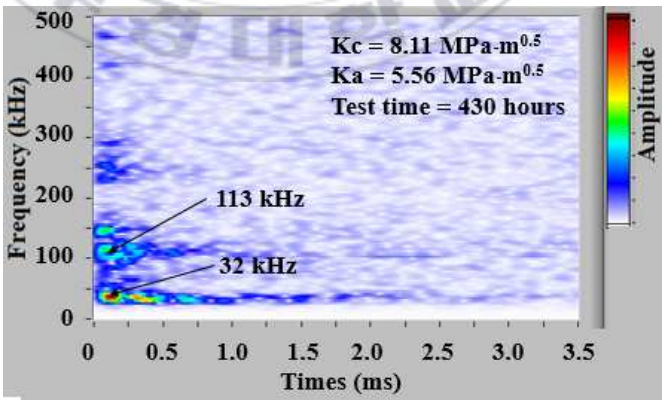

(c)

Fig. 3.4 Elastic wave signal obtained from 430 hours of $K_c = 8.11\ \mathrm{MPa}\sqrt{\mathrm{m}}$ and $K_a = 5.56\ \mathrm{MPa}\sqrt{\mathrm{m}}$. (a) Waveform, (b) Power spectrum, (c) Time-frequency analysis.

Fig. 3.5 shows the cumulative elastic wave obtained in the experiment, and the dominant frequency obtained in Figs. 3.3 and 3.4. The elastic wave showed no signal detection at about 0–21 hours, 74–138 hours, and 263–310 hours. These are the regions where the hydrogen aggregated at the slit tip. Elastic wave signals were detected at 21–74 hours, 138–263 hours, and 310–430 hours. These are the regions where HAC occurred and was propagated by hydrogen aggregation. A lot of elastic wave signals occurred by corrosion and HAC at 21–74 hours. This is because large stress acts on the slit, and crack due to HAC being initiated. This can be seen in Fig. 3.5. The dominant frequency of the elastic wave was detected in the low-frequency band f(1) of about 30–43 kHz, due to corrosion; and in the high-frequency band f(2) of about 59–150 kHz, due to crack occurrence and propagation.

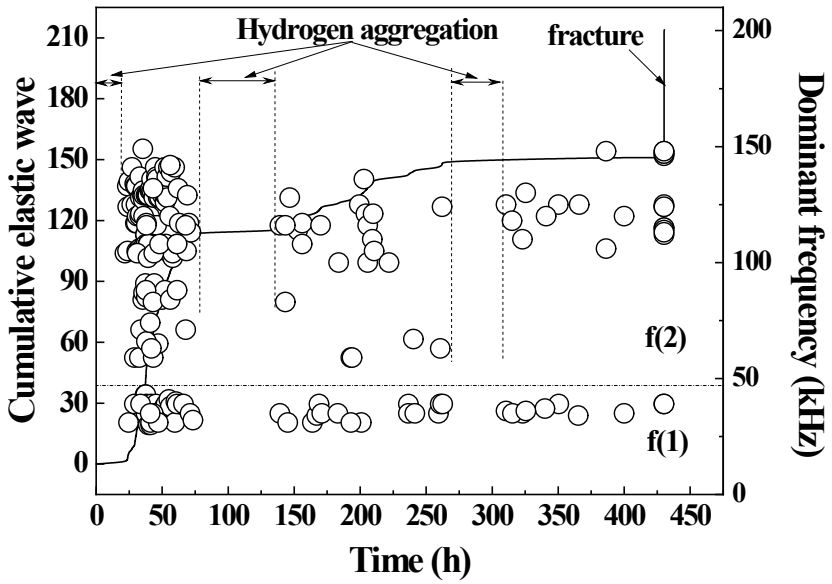

Fig. 3.5 Relationship of cumulative elastic wave, dominant frequency, and test time for $K_c = 8.11$ MPa$\sqrt{\text{m}}$ and $K_a = 5.56$ MPa$\sqrt{\text{m}}$.

Fig. 3.6 shows SEM image of the fracture surface after the experiment, where (a) shows the slit part of EDM, while (b)–(d) shows the slit tip portions where HAC has occurred. The HAC propagated due to a little corrosion and applied stress in the slit tip portion; (b) and (c) show enlarged images of the HAC portion. The grain boundary was embrittled, the grain was clearly observed, and cracks were observed in some cross-sections. In particular, (c) shows that crack has propagated towards the surface direction. It is judged that many elastic waves occurred in the 21–74 hours period during which stress was applied. The frequency band of about 40 kHz is the dominant frequency due to corrosion, and the frequency band above about 60 kHz is the dominant frequency due to crack occurrence and propagation.

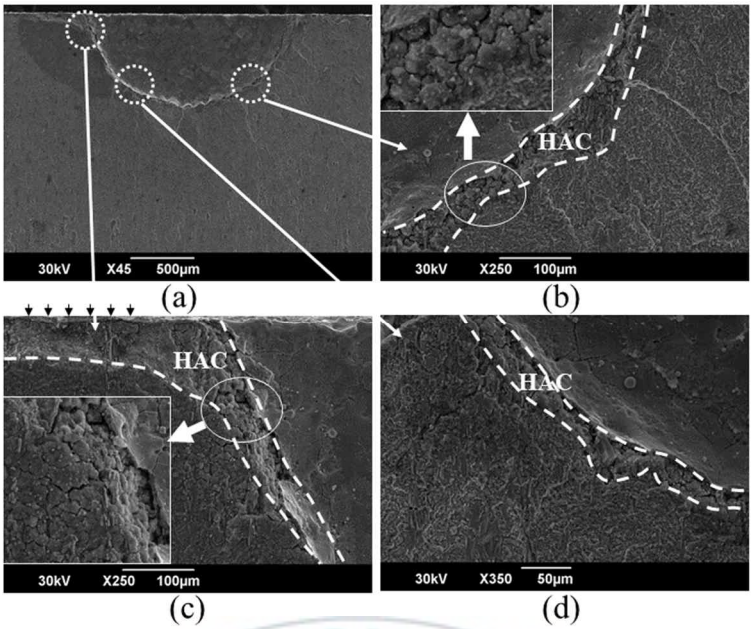

Fig. 3.6 SEM image from $K_c = 8.11$ MPa$\sqrt{\text{m}}$ and $K_a = 5.56$ MPa$\sqrt{\text{m}}$. (a) EDM slit, (b)–(d) slit–tip portion.

3.3.2 Elastic wave obtained from the stress intensity factor K_c=3.02M Pa$\sqrt{m}$ and K_a= 2.07 M Pa$\sqrt{m}$

Figs. 3.7 and 3.8 show the results of the waveform, frequency spectrum, and time-frequency analysis obtained when stresses are applied to the surface crack. Figs. 3.7 and 3.8 show the results obtained at 21 and 283 hours, respectively. In each figure, (a) is the waveform, (b) is the power spectrum, and (c) is the time-frequency analysis.

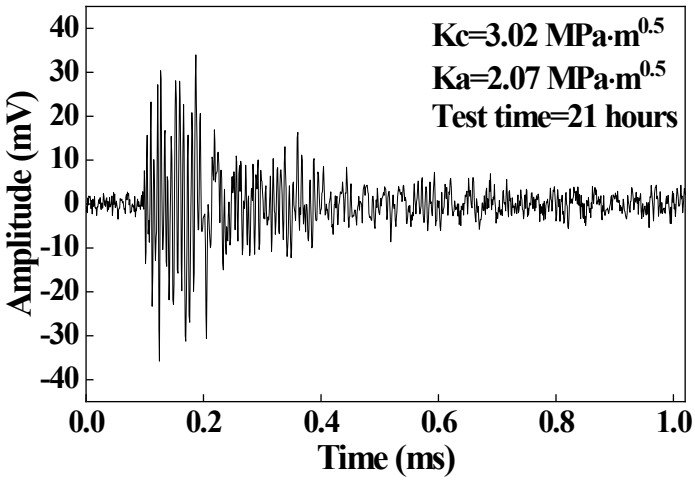

(a)

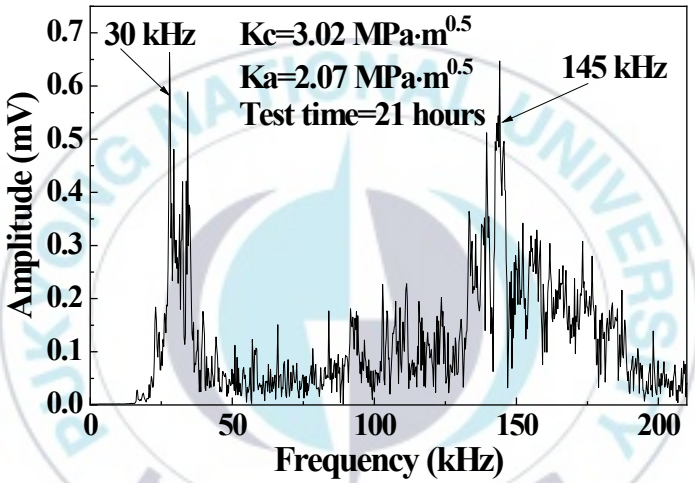

(b)

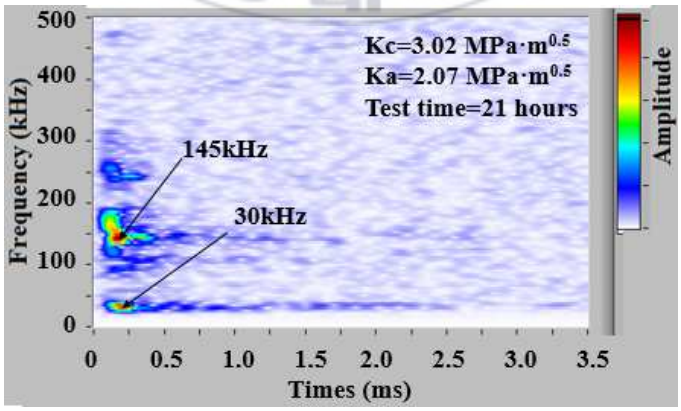

(c)

Fig. 3.7 Elastic wave signal detected from 21 hours of $K_c = 3.02\ \mathrm{MPa}\sqrt{\mathrm{m}}$ and $K_a = 2.07\ \mathrm{MPa}\sqrt{\mathrm{m}}$. (a) Waveform, (b) Power spectrum, (c) Time-frequency analysis.

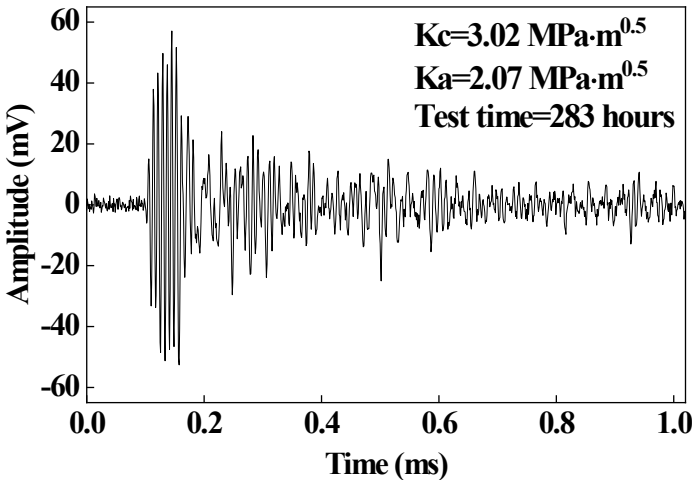

(a)

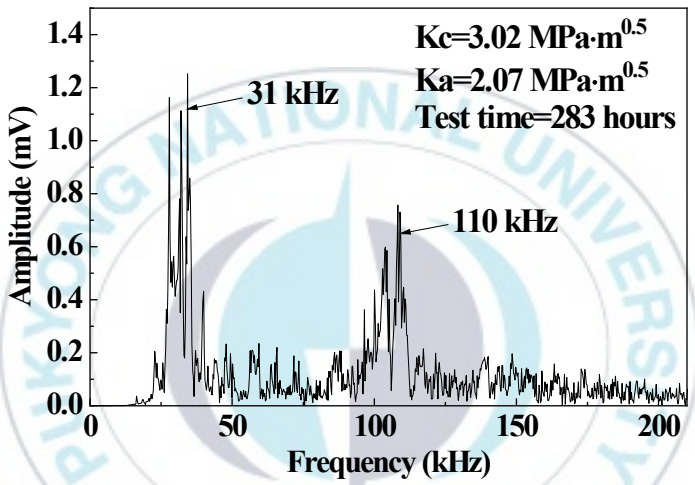

(b)

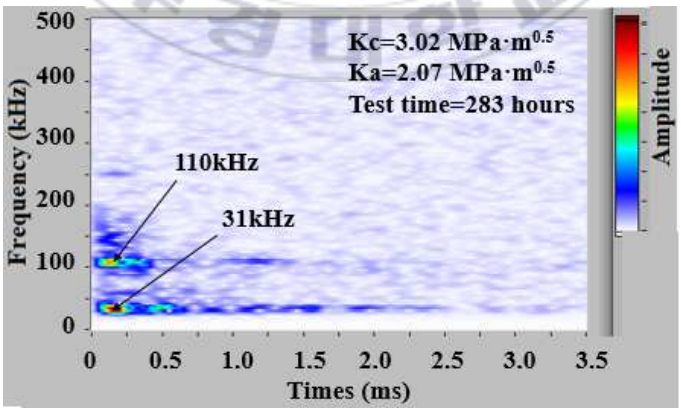

(c)

Fig. 3.8 Elastic wave signal detected from 283 hours of $K_c = 3.02$ MPa$\sqrt{\text{m}}$ and $K_a = 2.07$ MPa$\sqrt{\text{m}}$. (a) Waveform, (b) Power spectrum, (c) Time-frequency analysis.

Fig. 3.9 shows the cumulative elastic wave obtained in the experiment and the dominant frequency obtained in Figs. 3.7 and 3.8, in which (a) shows the whole up to about 500 h, while (b) shows the enlarged plot up to 282 h. The elastic wave had no signal detection at about 0–18 hours, 63–135 hours, and 235–282 hours. These are the regions where the hydrogen aggregated at the slit tip. Elastic wave signals were detected at 18–63 hours, 135–235 hours, and after 282 hours. This is the region where HAC occurred and has propagated by hydrogen aggregation. The dominant frequency of the elastic wave was detected in the low-frequency band f(1) of about 32–40 kHz due to corrosion and in the high-frequency band f(2) of about 59–177 kHz due to crack occurrence and propagation. The frequency after 282 hours is about 32 kHz, which is an elastic wave due to corrosion.

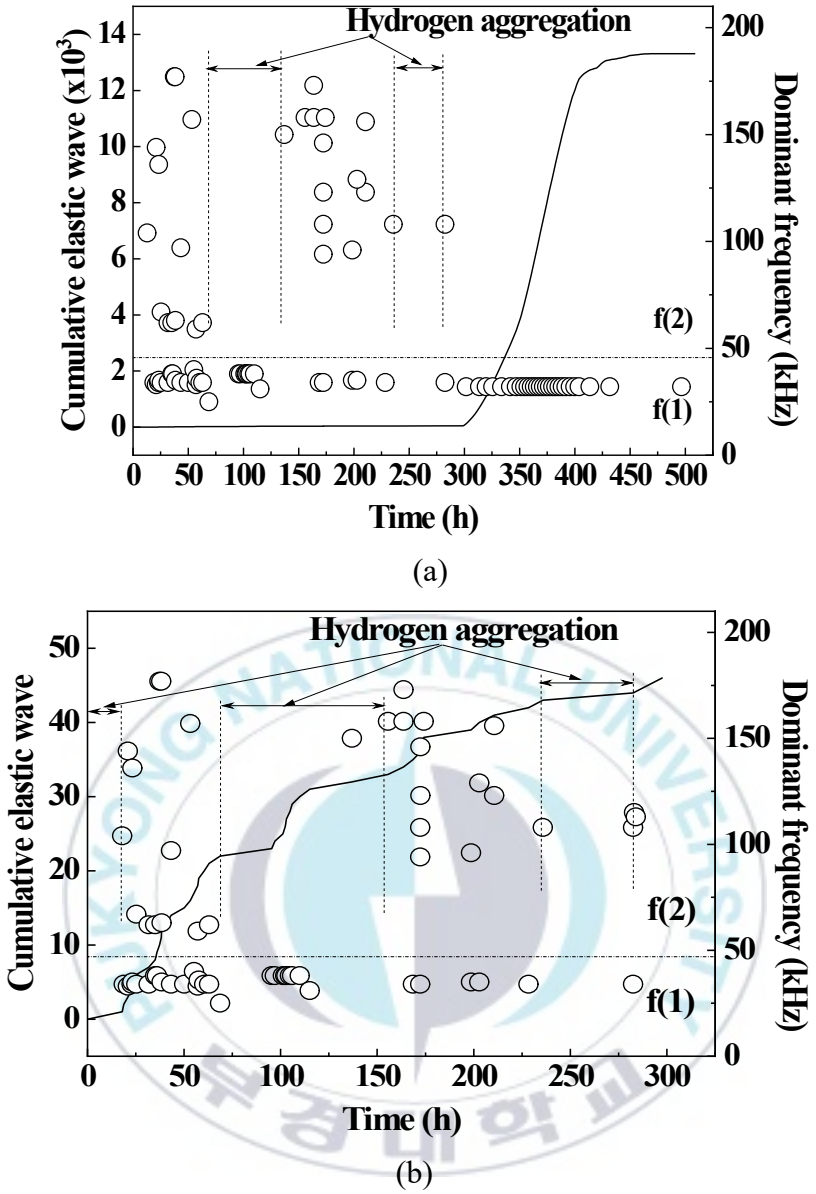

Fig. 3.9 (a) Relationship of cumulative elastic wave, dominant frequency, and test time for $K_c = 3.02\ \mathrm{MPa}\sqrt{\mathrm{m}}$ and $K_a = 2.07\,\mathrm{MPa}\sqrt{\mathrm{m}}$. (b) Magnification of 0–282 hours.

Fig. 3.10 shows SEM image of the fracture surface after the experiment, where (a) shows the slit part of EDM, and (b)–(d) are the slit tip portions where HAC has occurred. The HAC propagated due to a little corrosion and applied stress in the slit tip portion; (b)–(d) show enlargements of the HAC portion. The grain boundary is embrittled, the grain is clearly observed, and cracks are observed in some cross-sections. The low-frequency band f(1) of about 40 kHz is the dominant frequency due to corrosion, while the high-frequency band f(2) above about 60 kHz is the dominant frequency due to crack occurrence and propagation.

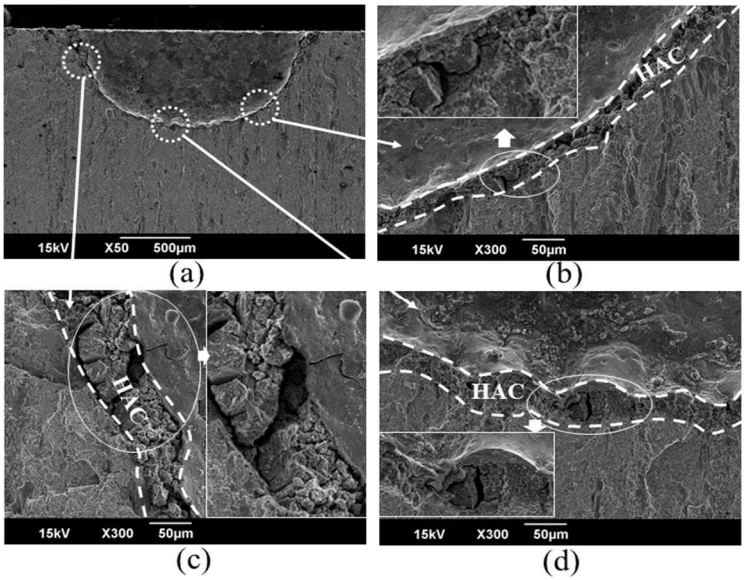

Fig. 3.10 SEM image from $K_c = 3.02$ MPa$\sqrt{\text{m}}$ and $K_a = 2.07$ MPa$\sqrt{\text{m}}$. (a) EDM slit, (b)–(d) slit–tip portion.

3.3.3 Elastic wave obtained from the stress intensity factor $K_c=2.86 MPa\sqrt{m}$ and $K_a=1.96 MPa\sqrt{m}$

Fig. 3.11 shows the results of the waveform, frequency spectrum, and time-frequency analysis obtained when stresses, such as the stress intensity factor $K_c=2.86\ MPa\sqrt{m}$ and $K_a=1.96\ MPa\sqrt{m}$ are applied to the surface crack. Fig. 3.11 is the result obtained at 168 hours; in each figure, (a) is the waveform, (b) is the power spectrum, and (c) is the time-frequency analysis.

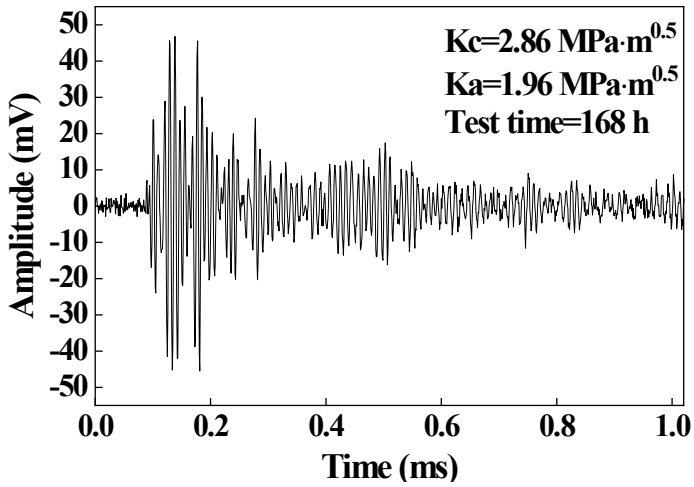

(a)

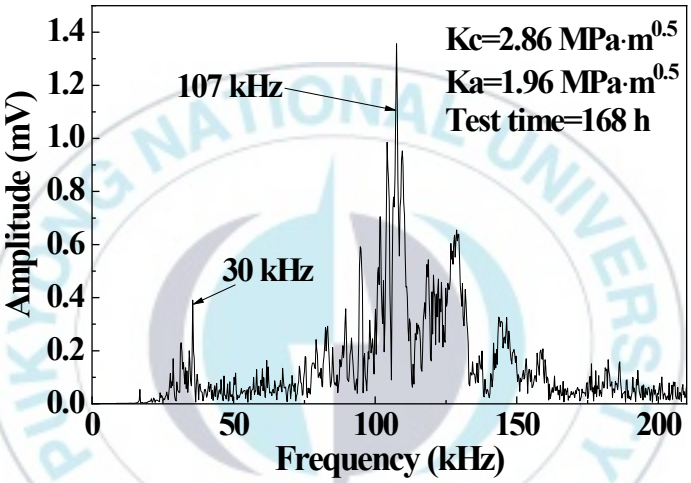

(b)

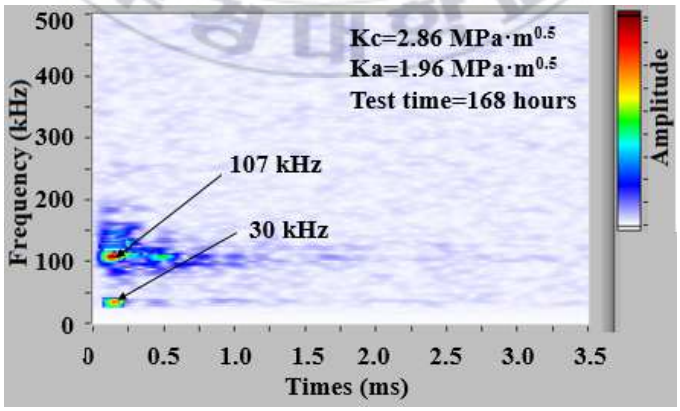

(c)

Fig. 3.11 Elastic wave signal detected from 168 hours of $K_c = 2.86$ MPa$\sqrt{\text{m}}$ and $K_a = 1.96$ MPa$\sqrt{\text{m}}$. (a) Waveform, (b) Power spectrum, (c) Time-frequency analysis.

Fig. 3.12 shows the cumulative elastic wave obtained in the experiment and the dominant frequency obtained in Fig. 3.11. Even though this specimen was tested for 320 hours, no valid signal was detected from 240 hours. No elastic wave signals were detected at about 0–160 hours and 180–238 hours. These are the regions where the hydrogen aggregated at the slit tip. The elastic wave signal was detected at 160–180 hours and 238–239 hours. These are the regions where HAC has occurred and is propagated by hydrogen aggregation. Less elastic waves occurred in this specimen than in others specimen. A slight elastic wave was detected in the low-frequency band f(1) of about 30 kHz due to corrosion and in the high-frequency band f(2) of about 100–150 kHz due to crack occurrence and propagation. The reason why a slight signal was detected can be observed in the fracture surface of Figure 3.13.

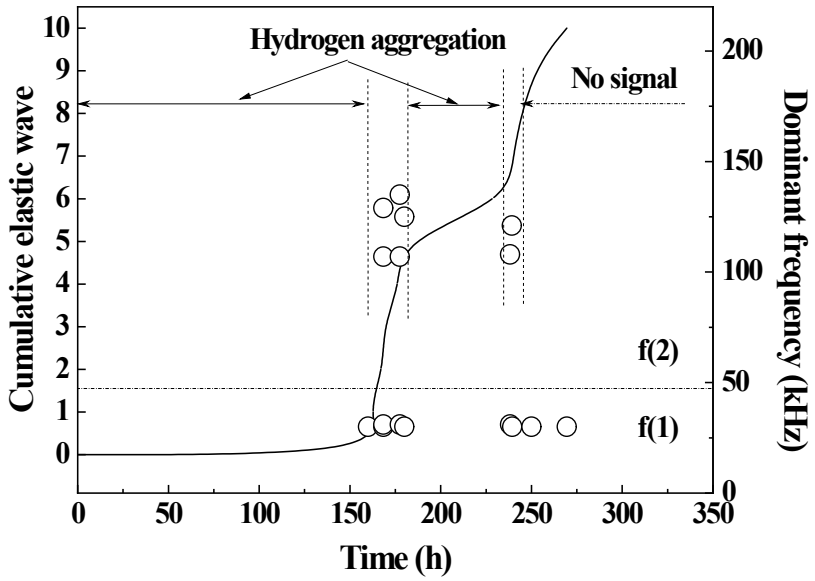

Fig. 3.12 Relationship of cumulative elastic wave, dominant frequency, and test time for $K_c = 2.86\ \mathrm{MPa}\sqrt{\mathrm{m}}$ and $K_a = 1.96\ \mathrm{MPa}\sqrt{\mathrm{m}}$.

Fig. 3.13 shows SEM image of the fracture surface after the experiment, in which (a) shows the slit part of EDM, and (b) and (c) shows the slit surface where HAC occurred, while (d) shows the deepest part of the slit. A little HAC occurred in the surface side of the slit, due to corrosion and bending stress. However, crack propagation was not evident in the deepest part of the slit (d). Due to this phenomenon, a slight elastic wave during the initial crack occurrence portion was detected due to corrosion, and after 240 hours, was not detected. Therefore, the HAC threshold stress intensity factor (K_{IHAC}) of the surface crack specimen used in this study was determined to be $K_{IHAC} = 1.96\text{MPa}\sqrt{\text{m}}$.

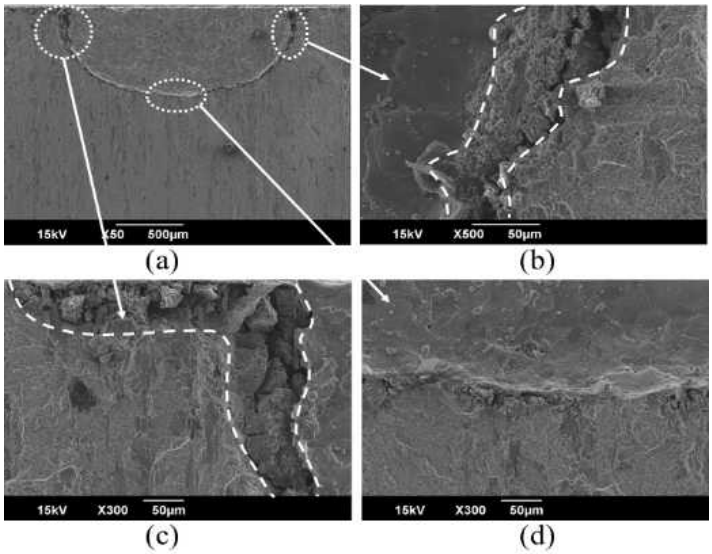

Fig. 3.13 SEM image from $K_c = 2.86$ MPa$\sqrt{\text{m}}$ and $K_a = 1.96$ MPa$\sqrt{\text{m}}$. (a) EDM slit, (b)~(d) slit–tip part.

Fig. 3.14 shows the relationship between hydrogen aggregation time and elastic wave detection time according to the stress intensity factor of the slit surface. In the figure, the square symbol (□) shows the hydrogen aggregation time, while the circle symbol (○) shows the elastic wave detection time. It is evident that as K_c becomes smaller, the hydrogen aggregation time becomes longer, and the elastic wave detection time becomes shorter. When K_c is large, large stress acts on the slit tip, so that HAC occurs rapidly, and the time of elastic wave occurrence becomes long. However, when K_c is small, it takes a long time for HAC to occur due to the application of small stress on the slit tip, and the time of elastic wave occurrence is shortened. As described above, the occurrence time of HAC differed according to the applied stress.

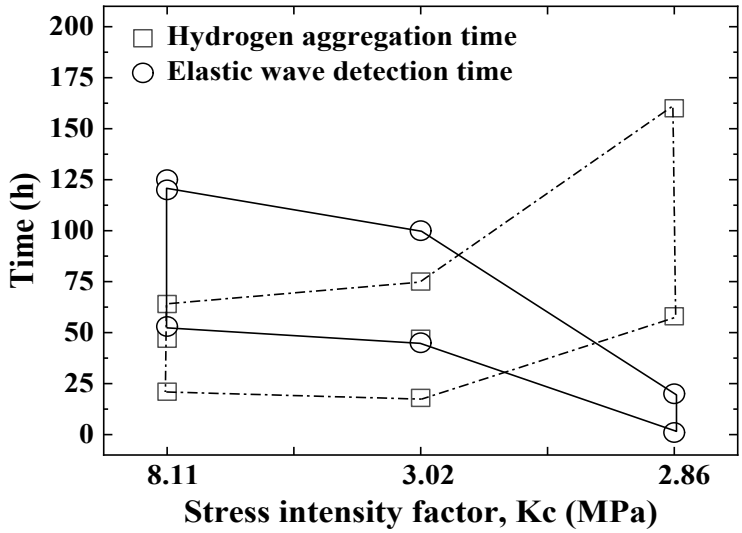

3.4 Summary

This chapter analyzed the elastic wave properties of hydrogen-assisted cracking (HAC) of ultra-high-strength steel (SKD11: HV670) under different loads in a solution of acetic acid 0.057M and determined the threshold stress intensity factor (K_{HAC}).

1) The frequency band of the elastic wave was divided into dominant frequency below about 50 kHz and above about 60 kHz, regardless of the value of K_c. The low-frequency band below about 50 kHz is the elastic wave due to corrosion, while the high-frequency band above about 60 kHz is the elastic wave caused by crack occurrence and propagation.
2) In the acetic acid solution atmosphere, as K_c becomes smaller, the hydrogen aggregation time of the slit tip becomes longer, the elastic wave detection time becomes shorter, and slight elastic waves are detected.
3) The fracture surface due to the static bending stress acting on the end of the cantilever beam showed the shape by corrosion and HAC. In the crack propagation part, grain boundaries were embrittled by corrosion, and grains were clearly observed. In some zones, cracks were observed in the cross-section.
4) When K_c was the smallest, the crack in the surface direction propagated slightly, but the crack in the depth direction did not propagate at all. The stress intensity factor at this time was determined as the HAC threshold stress intensity factor(K_{HAC}). That is, K_{HAC} was determined to be $1.96\ \mathrm{MPa}\sqrt{\mathrm{m}}$.
5) HAC can be prevented by minimizing contact between the high-strength metal and hydrogen. However, when HAC occurs, it can be monitored through elastic wave detection.

References

1. B. Meng, C. Gu, L. Zhang, C. Zhou, X. Li, Y. Zhao, J. Zheng, X. Chen, and Y. Han, Hydrogen effects on X80 pipeline steel in high-pressure natural gas/hydrogen mixtures, Int J Hydrogen Energy, 42 (2017) 7404-7412.

2. N. E. Nanninga, Y. S. Levy, E. S. Drexler, R. T. Condon, A. E. Stevenson, and A. J. Slifka, Comparison of hydrogen embrittlement in three pipeline steels in high pressure gaseous hydrogen environments, Corrosion Science, 59 (2012) 1-9.

3. C. F. Dong, Z. Y. Liu, X. G. Li, and Y. F. Cheng, Effects of hydrogen-charging on the susceptibility of X100 pipeline steel to hydrogen-induced cracking, Int J Hydrogen Energy, 34 (2009) 9879-9884.

4. X. Tang and Y. F. Cheng, Quantitative characterization by micro-electrochemical measurements of the synergism of hydrogen, stress and dissolution on near-neutral pH stress corrosion cracking of pipelines, Corrosion Science, 53 (2011) 2927-2933.

5. W. Zhao, T. Zhang, Z. He, J. Sun, and Y. Wang, Determination of the critical plastic strain-induced stress of X80 steel through an electrochemical hydrogen permeation method, Electrochimica Acta, 214 (2016) 336-344.

6. A. R. Troiano, The Role of Hydrogen and Other Interstitials in the Mechanical Behavior of Metals, Trans ASM, 52 (1960) 54–80.

7. R. A. Oriani and P. H. Josephic, Equilibrium aspects of hydrogen-induced cracking of steels, Acta Metallurgia, 22 (1974) 1065-1074.

8. R. A. Oriani and P. H. Josephic, Equilibrium and kinetic studies of the hydrogen-assisted cracking of steel, Acta Metalurgica, 25 (1977) 979-988.

9. W. W. Gerberich, Y. T. Chen, and C. St. John, Hydrogen-controlled cracking - An approach to threshold stress intensity, Metall Trans A, 6A (1975) 1485-1498.

10. R. L. S. Thomas, J. R. Scully, and R. P. Gangloff, Internal hydrogen embrittlement of ultrahigh-strength AERMET 100 steel, Metall Mater Trans A, 34 (2003) 327-344.

11. W. W. Gerberich, T. Livne, X. F. Chen, and M. Kaczorowski, Crack growth from internal hydrogen - Temperature and microstructural effects in 4340 steel, Metall Trans A, 19A (1988) 1319-1334.

12. C. J. McMahon Jr., Hydrogen-induced intergranular fracture of steels, Eng Fract Mech, 68 (2001) 773-788.

13. D. Symons, A comparison of internal hydrogen embrittlement and hydrogen environment embrittlement of X-750, Eng Fract Mech, 68 (2001) 751-771.

14. R. L. S. Thomas, J. R. Scully, and R. P. Gangloff, Internal hydrogen embrittlement of ultrahigh-strength AERMET 100 steel, Metall Mater Trans A, 34A (2003) 327-344.

15. R. P. Gangloff, Comprehensive Structural Integrity-Environmentally Assisted Failure, Elsevier Ltd, Oxford, United Kingdom, (2003) 31-101.

16. C. D. Beachem, A new model for hydrogen-assisted cracking (hydrogen "embrittlement"), Metall. Trans., 3 (1972) 437-451.

17. J. P. Hirth, Effects of hydrogen on the properties of iron and steel, Metall Trans A, 11A (1980) 861-890.

18. Y. Takeda and C. J. McMahon Jr., Strain controlled vs stress controlled hydrogen induced fracture in a quenched and tempered steel, Metall Trans A, 12A (1981) 1255-1266.

19. M. Gao and R. P. Wei, Hydrogen partitioning model for hydrogen assisted crack growth, Metall Trans A, 16A (1985) 2039-2050.

20. S. P. Lynch, Hydrogen effects on materials behavior and corrosion deformation interactions, TMS, Warrendale, PA, (2003) 449-466.

21. R. P. Gangloff and A. Turnbull, Modeling environmental effects on crack initiation and propagation, TMS, Warrendale, PA, (1986) 55-81.

22. R. P. Gangloff, Comprehensive structural integrity-environmentally assisted failure, Elsevier Ltd, Oxford, United Kingdom, (2003) 31–101.

23. Y. Lee and R. P. Gangloff, Measurement and modeling of hydrogen environment–

assisted cracking of ultra-high-strength steel, Metall Mater Trans A, 38A (2007) 2174-2190.

24. S. P. Lynch, Mechanistic and fractographic aspects of stress corrosion cracking, Corrosion Reviews, 30 (2012) 63-104.

25. A. Nagao, C. D. Smith, M. Dadfarnia, P. Sofronis, and I. M. Robertson, Interpretation of hydrogen-induced fracture surface morphologies for lath martensitic steel, Procedia Materials Science, 3 (2014) 1700-1705.

26. R. P. Gangloff, H. M. Ha, J. T. Burns, and J. R. Scully, Measurement and modeling of hydrogen environment-assisted cracking in Monel K-500, Metall Mater Trans A, 45A (2014) 3814–3834.

27. L. F. Li, Z. Zhang, G. T. Shen, and Z. W. Wu, Acoustic emission as a technique to study hydrogen induced cracking behavior of low-carbon steel, 3rd International Congress on Image and Signal Processing (CISP2010), (2010) 4002-4005.

28. D. S. Bae, J. K. Lee, S. P. Lee, I. S. Son, U. B. Baek, S. H. Nahm, J. H. Lee, Evaluation on hydrogen embrittlement of material using nondestructive test, Int J Precision Engng Manufacturing, 15 (2014) 989-993.

29. J. C. Newman Jr and I. S. Raju, An empirical stress-intensity factor equation for the surface crack, Eng Fract Mech, 15 (1981) 185-192.

Chapter 4

Evaluation of Fatigue Life of Ultra-High Strength Steel Under Stress Corrosion Environment

4.1 Introduction

Ultra-high strength steel (UHSS) is developed for lightweight structures. When these structures are exposed to a hydrogen atmosphere and applied with acidic substances and stress, hydrogen embrittlement occurs, in which the mechanical properties are degraded due to the hydrogen attack on the microstructures. Hydrogen-assisted cracking (HAC) is likely to occur in UHSS. McEvily et al. [1] reviewed a number of case studies involving HAC in steel. HAC is based on bond weakening and strain localization. Beachem [2] presented HAC based on an observed decrease in microscopic plasticity and changes in fracture modes with decreasing stress intensities at crack tips during the stress-corrosion cracking and HAC of quenched and tempered steels. He suggested that the presence of sufficiently concentrated hydrogen dissolved in the lattice immediately ahead of the crack tip aids the deformation of the microstructure. Van Leeuwen [3] developed equations describing the diffusion to and the subsequent precipitation of hydrogen into lenticular voids resulting from the stress-induced decohesion of grain boundary precipitates. Oriani et al. [4] investigated the direct and important effects of hydrogen on the decohesioning mode at regions directly at the crack tip and at regions of high stress due to dislocation interactions within the plastic enclave. Briant [5] reported that the most detrimental effect of increasing the susceptibility of a material to hydrogen cracking is the formation of martensite upon deformation. Gerberich et al. [6] investigated the effects of internal hydrogen on stage II crack growth rates in AISI 4340 steel as a function of test temperature. McMahon [7] reported that the hydrogen-induced intergranular brittle fracture of steels is caused by a combination of hydrogen dissolved in the crystal lattice and embrittling impurities that had previously segregated at grain boundaries. Symons [8] reported that degradation due to hydrogen can be classified into two categories: internal hydrogen embrittlement and hydrogen environment embrittlement. Thomas et al. [9] and

Lee et al. [10] explained hydrogen embrittlement based on ultra-high-strength AERMET 100. Meng et al. [11] reported that X80 pipeline steel is susceptible to hydrogen-induced embrittlement in natural gas/hydrogen mixtures, and that hydrogen embrittlement susceptibility increases with the hydrogen partial pressure. Additionally, the hydrogen embrittlement susceptibility depends on the textured microstructure caused by hot rolling, particularly for notch specimens. Calculation based on measured fatigue data revealed that the fatigue life of an X80 steel pipeline was degraded substantially by the added hydrogen. HAC was not observed below the threshold stress intensity factor (K_{IHAC}) [12], and the crack growth rate was indicated above K_{IHAC}.

Haddad et al.[13] proposed an equation to evaluate the fatigue limit of microcracked materials. Kitagawa et al. [14] experimentally demonstrated that the threshold stress intensity factor range of the fatigue crack propagation for microcracks decreased as the crack length shortened. Tange et al. [15] suggested by modification of Haddad's equation. Ando et al. [16] was proposed the equation that focuses on nonlinear behavior at the fatigue limit, which is substantially lower than the yield stress. It was possible to quantitatively evaluate the fatigue limit according to the size of microcracks using the Ando et al. equation. Therefore, it is necessary to review the applicability of the fatigue limit evaluation according to the size of microcracks in the corrosive environments.

In this study, Static fatigue limit of HV670 (UHSS) in a corrosive environment for preventing structural fracture due to HAC were evaluated from experimental and calculation. The static fatigue limit based on the crack depth was determined using K_{IHAC}. This result can be applied to the fatigue limit evaluation of UHSS under corrosive environments and data for securing the stability of chemical plants.

4.2 Material and experimental method

4.2.1 Specimen

SKD11, which was heat treated to obtain UHSS for the HAC experiments, was used as the material for cold mold steel. The heat-treatment conditions were as follows: quenching at 1,036 °C for 2 h, and tempering at 180 °C. The Vickers hardness (HV) of the UHSS obtained by the heat treatment was 670. The fatigue limit of smooth specimen was used for 13 specimens. The fatigue limit of cracked specimen was used for 18 specimens. The crack was made at the smallest cross section of the specimen by electrical discharge machining. The crack aspect ratio (*a/c*) was 1.0. The crack depth (*a*) was 0.05, 0.1, and 0.2mm, respectively. Six specimens were experimented for each crack depth, and used total 18 specimens. Table 4.1 shows the chemical composition of SKD11. Fig. 4.1 shows the shape and dimensions of the specimen subjected to the HAC experiment. Three holes of ϕ6 on left side are for fixing the specimen. One hole of ϕ3 on right side is to operate the stress on the free end of the specimen. The round part of the R24 is to install the container to induce the HAC.

Table 4.1 Chemical compositions of SKD11. (wt.%)

C	Si	Mn	P	S	Ni	Cr	Mo	V
1.489	0.272	0.329	0.024	0.001	0.239	11.29	0.843	0.236

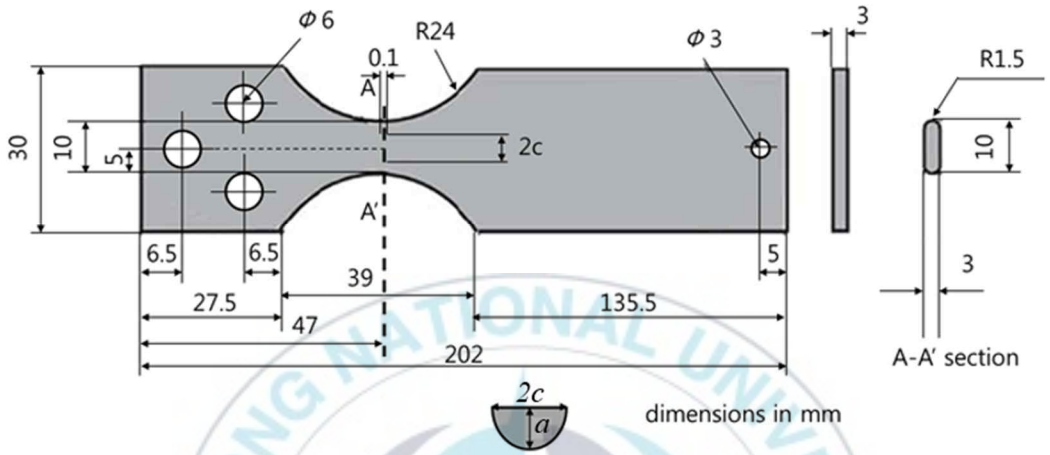

Fig. 4.1 Ultra-high strength steel specimen for HAC.

4.2.2 Determination of $K_{IH\,AC}$ based on elastic wave

The slit of the specimen was machined at the center with a width of 10 mm using electric discharge machining. The semicircular slit of the specimen for determining $K_{IH\,AC}$ was 2c = 1.4 mm. Meanwhile, the depth a = 0.7 mm, and the crack aspect ratio (a/c) = 1.0. The static loads applied to the free end of the specimen based on c and a are denoted as K_c and K_a, respectively, and they are calculated using the Newman–Raju equation [13].

The NI PXIe SYSTEM, which supports up to eight channels, was used to detect the waveform and frequency characteristics of the elastic wave signal. The detection sampling rate of the elastic wave was 1 MHz, and the sampling size was 4,096. The elastic wave detection sensor was a wideband sensor with a sampling rate of 1 MHz with a wide range of frequency response characteristics. The elastic wave was detected using a 28dB preamplifier. Time-frequency analysis of the detected elastic wave signal was performed using LabVIEW. Fig. 4.2 shows a schematic illustration of the experimental setup. The cross section of the specimen was observed using SEM.

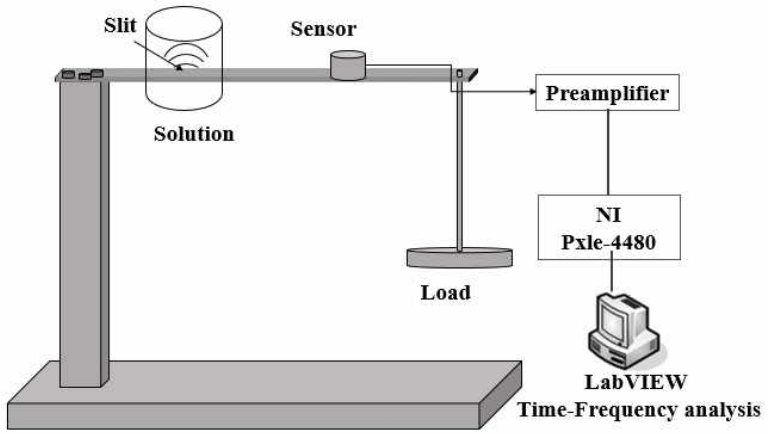

Fig. 4.2 Schematic illustration of experimental apparatus.

4.2.3 Determination of static fatigue limit

The smooth specimen, as shown in Fig. 4.1, was immersed in a 0.057M (pH 3) acetic acid solution. Acetic acid is primarily used in the products making as well as food industry. The wastewater containing acetic acid is discharged from chemical industries [17]. It cause water, soil and air pollution. This cause the HAC. Therefore, the HAC was simulated using the strong pH acetic acid. Static fatigue due to bending stress was imposed by applying a load to the free end. Fig. 2 shows a schematic illustration of the experimental setup.

4.2.4 Fatigue limit evaluation of stress corrosion cracking

To evaluate the fatigue limit of hydrogen-assisted stress corrosion cracking, semicircular slits with crack depths (a) of 0.1 and 0.2 mm were created via electric discharge machining. The crack aspect ratio (a/c) was set to 1.0.

The stress intensity factor (K) of a semi-elliptical surface crack of a finite plate can be evaluated using the Newman–Raju equation [18].

When the static fatigue bending stress (σ_B) is imposed on the semicircular surface crack of a finite plate, the dependence of the microcrack size of the threshold stress intensity factor $K_{IHAC(s)}$ can be evaluated using Eq. (4.1) [16].

$$K_{IHAC(s)} = 2\beta\sigma_w\sqrt{\frac{a}{\pi}}\cos^{-1}\left[\left\{\frac{\pi}{8\beta^2 a}\left(\frac{K_{th(l)}}{\sigma_w}\right)^2 + 1\right\}^{-1}\right] \qquad (4.1)$$

Here, $K_{IHAC(s)}$ is the threshold stress intensity factor for any microcrack size, and its value changes depending on the angle of the crack tip.

The fatigue limit (σ_{wc}) of microcracks in the finite plate can be obtained by substituting the $K_{IHAC(s)}$ obtained in Eq. (4.1) and the crack depth (a) into Eq. (4.2) [16].

$$K_{IHAC(s)} = \sigma_{wc}\sqrt{\pi a} \qquad (4.2)$$

4.2.5 Fracture surface observation

The fracture surfaces after static fatigue testing were examined using a scanning electron microscope (TESCAN (VEGA II LSU)).

4.3 Results and discussion

4.3.1 $K_{IHAC(s)}$

Stress was applied such that the stress intensity factor of the crack became $K_{IHAC(c)} = 2.86\ MPa\sqrt{m}$ and $K_{IHAC(a)} = 1.96\ MPa\sqrt{m}$ at the surface and depth, respectively [15]. Fig. 4.3 shows the waveform, frequency spectrum, and time–frequency analysis results obtained based on those values. Fig. 4.3 shows the results obtained at 268 hours. In each figure, (a) shows the waveform, (b) the power spectrum, and (c) the time–frequency analysis.

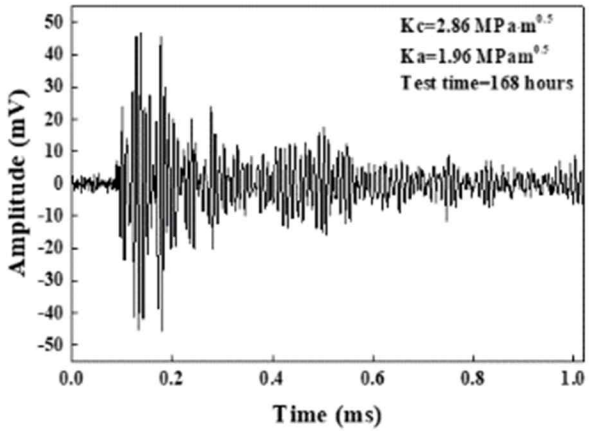

(a)

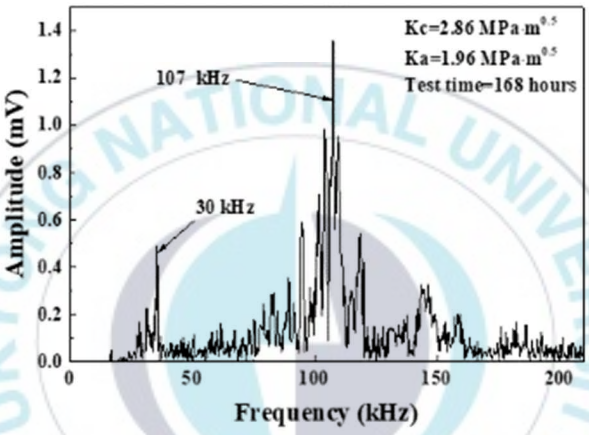

(b)

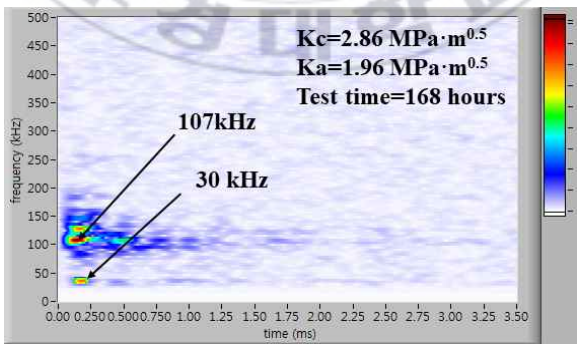

(c)

Fig. 4.3 Elastic wave signal detected from 21 hours of $K_{HAC\,(c)} = 2.86\ MPa\sqrt{m}$, $K_{HAC\,(a)} = 1.96\ MPa\sqrt{m}$. (a) Waveform, (b) power spectrum, (c) time–frequency analysis.

Fig. 4.4 shows the time based on the accumulated elastic wave obtained in the experiment and the dominant frequency obtained in Fig. 4.3. The specimen was tested for 320 hours, but no valid signal was detected after 240 hours; therefore, the test was stopped at 320 hours. The elastic wave signal was not detected at 0–160 hours and 180–238 hours. These time periods were considered as the hydrogen agglomeration time at the tip of the slit. The elastic wave signals were detected at 160–180 hours and 238–239 hours. At these time periods, HAC was initiated and propagated owing to hydrogen aggregation. As shown in Fig. 4.4, the elastic wave signal generated was less. However, a low-frequency band f(1) of approximately 30 kHz due to corrosion and a high-frequency band f(2) of 100–150 kHz due to crack initiation and propagation were detected. The less signal generated can be explained by the fracture surface shown in Fig. 4.5.

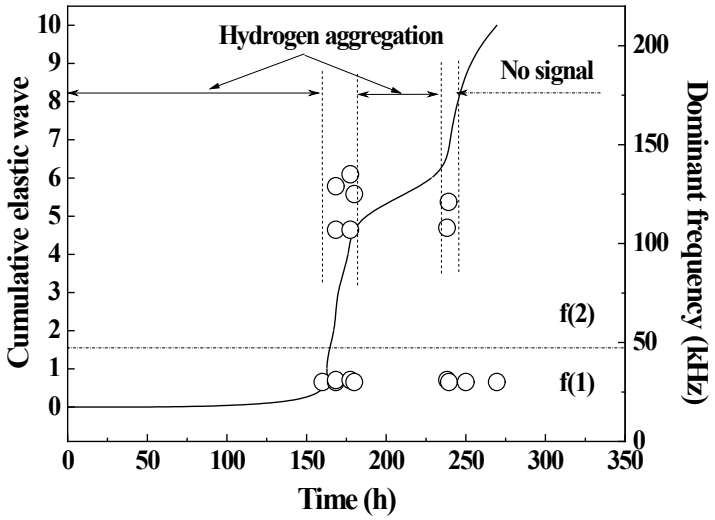

Fig. 4.4 Relationship of cumulative count between dominant frequency

Fig. 4.5 shows an SEM image of the fracture surface after the experiment. (a) shows the slit portion of the electric discharge machining. (b) and (c) show the slit surfaces where HAC occurred, and (d) shows the deepest section of the slit. At the tip of the slit, the crack of the HAC propagated slightly owing to the slight corrosion and applied bending stress. However, in the deepest section of the slit (d), no crack propagation was observed. Hence, no elastic wave signal was detected after 240 hours, and only a slight amount of elastic wave due to corrosion at the initial cracking area was detected.

Therefore, the K_{IHAC} of the surface crack specimen used in this study was determined as $K_{IHAC(a)} = 1.96\, M\, P\sigma\sqrt{m}$ based on the depth direction without crack propagation.

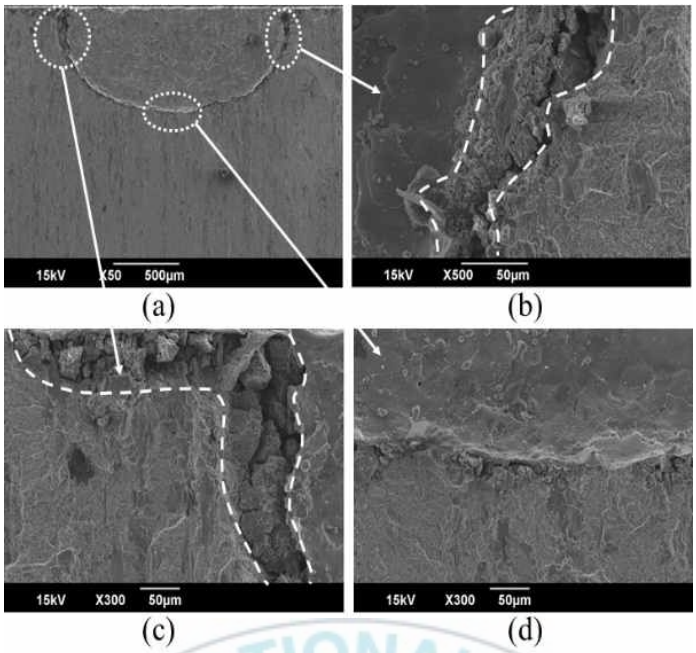

Fig. 4.5 SEM image from $K_{IHAC\,(c)} = 2.86\ MPa\sqrt{m}$, $K_{IHAC\,(a)} = 1.96\ MPa\sqrt{m}$. (a) EDM slit, (b)–(d) Slit-tip region.

4.3.2 Static fatigue limit of smooth specimen

The bending stress of the static fatigue was applied to the free end of the specimen immersed in the corrosion solution. Fig. 4.6 shows the relationship between the immersion time and the applied bending stress. It was discovered that when 580 MPa was applied, fracture occurred at 200 h; 550 MPa, 300 h; 500 MPa, 524.5 and 650 h; 450 MPa, 1132.5 h; 420 MPa, 984 h; 410 MPa, 1344 h. However, when 390, 400, and 410 MPa was applied, fracture did not occur at 2280, 2235, and 2260 h, respectively. Therefore, average 400 MPa was determined as the static fatigue limit of SKD11 (HV670).

This is small than about 600 MPa, the result of fully reversed, axial fatigue tests (R = -1) by Fukaura et al. [19]. In addition, it was smaller than the result of the ultrasonic fatigue testing machine under axial tension-compression with the stress ratio R = -1 by Akiniwa et al. [20]. The fatigue limit of SKD11-L and SKD11-T was approximately 480MPa and 580MPa, respectively. Since this was obtained at the stress ratio R = -1, it can be compared with the fatigue limit of this study as a positive value. The static fatigue limit of a corrosive environment is 69-83% the fatigue limit of the atmosphere. The results of this study show that the fatigue limit was small by HAC affect in a corrosive environment of strong acid. Therefore, in the corrosive environment where HAC occurs, the structure subject to fatigue load needs attention in design to ensure safety and reliability.

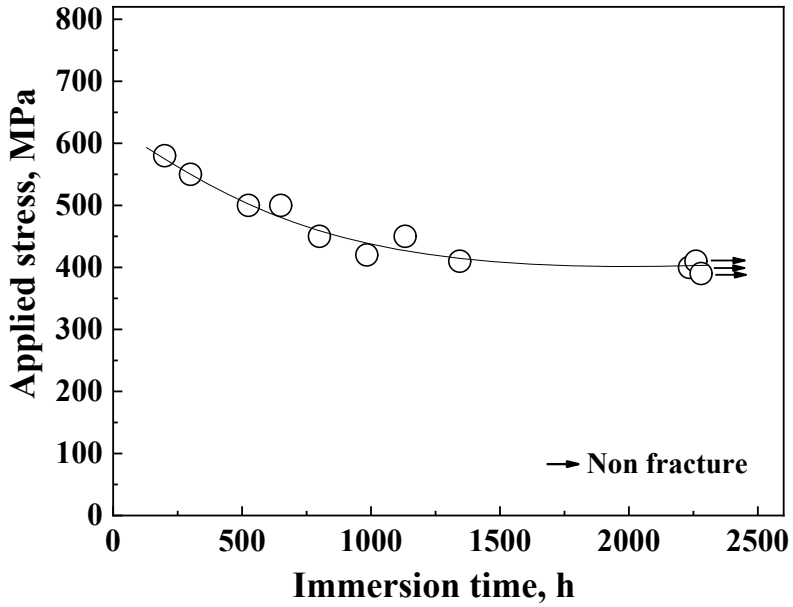

Fig. 4.6 Relationship between applied bending stress and immersion time.

4.3.3 Static fatigue limit of cracked specimen

Fig. 4.7 shows the static fatigue limit with respect to the crack depth. The solid line was obtained by substituting the static fatigue limit (400 MPa) obtained experimentally (solid line) and the threshold stress intensity factor $K_{IHAC\,(a)}$ = 1.96 MPa$\sqrt{m}$ based on the crack depth [21]. The results obtained from the static fatigue test and the calculation using Eq. (4.2) are shown in the figure. The solid line and circle symbol is results of calculation and test, respectively. The fatigue limit (solid line) of the crack specimen was almost constant up to a crack depth of 0.001 mm but decreased significantly thereafter. That is, the threshold stress at a microcracks approaches the fatigue limit of the material. The steep slope after 0.001mm converges to the threshold stress intensity factor of large crack. The under portion and the upper portion of the solid line in the figure indicate non-fracture and fracture, respectively. The open and solid symbols indicate non-fracture and fracture, respectively. Three non-fractures and three fractures were obtained for each crack depth (0.05, 0.1, and 0.2mm). The experimental results agreed well with the calculation results obtained using Eq. (4.2).

Eq. (4.2) can evaluate the fatigue limit of microcrack even under the condition that HAC occurs under stress corrosive environment using static fatigue limit and the threshold stress intensity factor K_{IHAC} . Eq. (4.2) evaluated the fatigue limit of microcracks regardless of the steel type [22,23]. Therefore, the fatigue limit of the structure in service can be evaluated with the crack size detected by nondestructive inspection, and the safety of the structure can be secured. The fatigue limit of the crack specimen is highly dependent on the material properties, the threshold stress intensity factor of the long crack and the fatigue limit of the smooth specimen. When the threshold stress intensity factor and the fatigue limit of the smooth material are small, the crack size which converges to fatigue limit of the smooth specimen have the large. That is, the crack size of STS316L is larger than that of SUP9A [22].

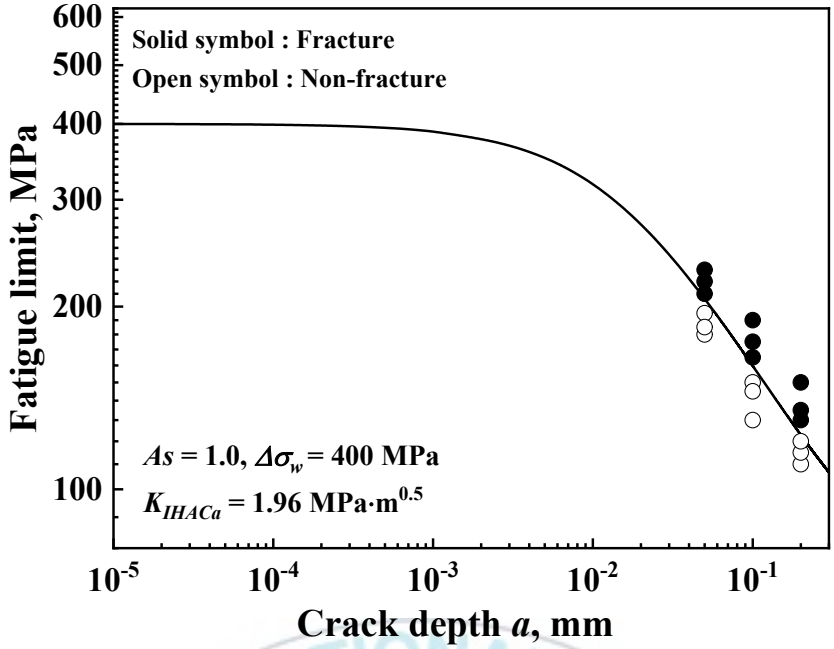

Fig. 4.7 Relationship between fatigue limit and crack depth.

Fig. 4.8(a)(b) shows the fracture surface of depth (a) of 0.2 mm obtained in the static fatigue experiment. (a) shows the fracture that occurred under a stress of 150 MPa. (b) shows a non-fractured surface under a stress of 110 MPa. The fracture surface (a) showed slight pitting on the surface, and the slit surface was corroded significantly. The fracture began from the slit, and the fracture surface exhibited a large trough. The surface shown in (b) was fractured owing to a large stress, and the slit surface was corroded.

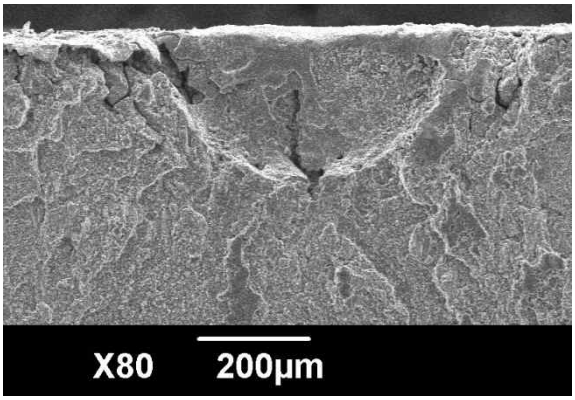

(a)

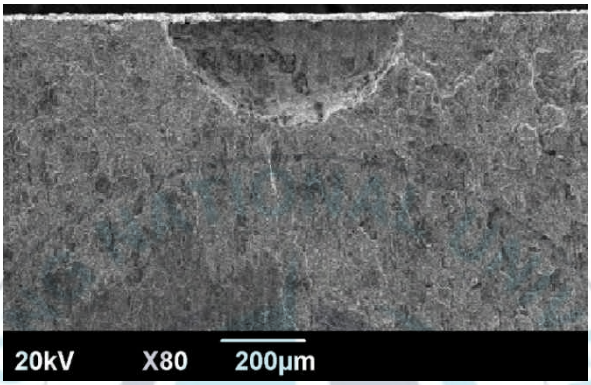

(b)

Fig. 4.8 Images of surfaces after static fatigue test. (a) Fracture, (b) non-fracture.

4.4 Summary

In this study, the elastic wave characteristics and $K_{IHAC(s)}$ for HAC were determined by immersing UHSS (SKD11: HV670) in a solution of acetic acid 0.057M (pH 3). In addition, the behavior of HAC was confirmed, and the static fatigue limit of a smooth specimen and the static fatigue limit of microcracks were evaluated.

1) The frequency band of the elastic wave was partitioned into a dominant frequency of approximately 50 kHz or less and approximately 60 kHz or more. The low-frequency band of approximately 50 kHz or less indicated an elastic wave due to corrosion, and the high-frequency band of approximately 60 kHz or more indicated an elastic wave due to crack initiation and propagation by HAC.
2) The fracture surface due to static fatigue bending stress exerting on the tip of the cantilever indicated corrosion and HAC. In the crack propagation portion, the grain boundaries were embrittled by corrosion, and grains were clearly observed. In some cases, cracks appeared on the fracture surface.
3) The HAC threshold stress intensity factor when cracks in the surface propagated slightly but not along the depth was determined to be $K_{IHAC(a)} = 1.96\ MPa\sqrt{m}$.
4) The static fatigue limit of UHSS (SKD11:HV670) was determined to be 400 MPa, and the static fatigue limit of the crack specimen can be evaluated using Eqs. (2) and (3). The experimental results agreed well with the evaluation results.

References

1. A. J. McEvily, I Le May, Hydrogen-assisted cracking, Materials Characterization,26 (1991) 253-268.
2. C. B. Beachem, A new model for hydrogen-assisted cracking (hydrogen "embrittlement", Metallurgical and Materials Transactions B, 3 (1972) 441-455.
3. H. P. Van Leeuwen, A Quantitative Model of Hydrogen Induced Grain Boundary Cracking , Corrosion, 29 (1973) 197–204.
4. R. A. Oriani and P. H. Josephic, Equilibrium and kinetic studies of the hydrogen-assisted cracking of steel, Acta Metalurgica, 25 (1977) 979-988.
5. C. L. Briant, Hydrogen assisted cracking of type 304 stainless steel, Metallurgical Transactions A, 10 (1979) 181–189
6. W. W. Gerberich, T. Livne, X. F. Chen, M. Kaczorowski, Crack growth from internal hydrogen—Temperature and microstructural effects in 4340 steel, Metallurgical and Materials Transactions A, 19 (1988) 1319-1334.
7. C. J. McMahon Jr., Hydrogen-induced intergranular fracture of steels, Engineering Fracture Mechanics, 68 (2001) 773-788.
8. D. Symons, A comparison of internal hydrogen embrittlement and hydrogen environment embrittlement of X-750, Engineering Fracture Mechanics, 68 (2001) 751-771.
9. R. L. S. Thomas, J. R. Scully and R. P. Gangloff, Internal hydrogen embrittlement of ultrahigh-strength AERMET 100 steel, Metallurgical and Materials Transactions A, 34 (2003) 327-344.
10. Y. Lee, R. P. Gangloff, Measurement and modeling of hydrogen environment-assisted cracking of ultra-high-strength steel, Metallurgical and Materials Transactions A, 38 (2007) 2174-2190.
11. B. Meng, C. Gu, L. Zhang, C. Zhou, X. Li, Y. Zhao, J. Zheng, X. Chen and Y. Han. Hydrogen effects on X80 pipeline steel in high-pressure natural gas/hydrogen mixtures, International Journal of Hydrogen Energy, 42 (2017) 7404-7412.
12. R. P. Gangloff, Comprehensive Structural Integrity-Environmentally Assisted Failure, Elsevier Ltd, Oxford, United Kingdom, (2003) 31-101.
13. J. C. Newman Jr, I. S. Raju, An Empirical Stress-Intensity Factor Equation for the

Surface Crack, Engineering Fractured Mechanics, 15 (1981) 185-192.
14. K. Ando, R. Fueki, K. W. Nam, K. Matsui, K. Takahashi, A Study on the Unification of the Threshold Stress Intensity Factor for Micro Crack Growth, Japan Society of Spring Engineers, 64 (2019) 39-44.
15. K. S. Lee, J. E. Paeng, K. G. Gu, K. W. Nam, Threshold stress intensity factor of ultra-high strength steel (HV670) containing surface crack by hydrogen assisted cracking and cumultive elastic wave, Journal of Mechanical Science and Technology, 35 (2021) 2441-2447.

Chapter 5
Conclusions

The elastic waves generated in ultra-high strength steel (UHSS) under various corrosive solutions were investigated. The threshold stress intensity factor (K_{IHAC}) for HAC was obtained from ultra-high strength steel (SKD11: HV670) by applying different loads in a solution of 0.057M acetic acid. The frequency characteristics by hydrogen aggregation and crack propagation were analyzed by the time-frequency analysis method using LabVIEW. The K_{IHAC} of the specimen was determined from the cumulative elastic wave and fracture surface, and the static fatigue limit based on the crack depth was determined using K_{IHAC}.

1. Regardless of the corrosion solution, elastic waves in a low frequency band, less than 40 kHz, and in a high frequency band, more than 60 kHz, were obtained.
2. The low frequency below 40 kHz was caused by corrosion, while the high frequency above 60 kHz are caused by crack initiation and propagation.
3. The elastic wave in the specimens under the acetic acid solution were caused by HAC-induced crack propagation, but the elastic wave in the specimens under 1.5M H_2SO_4 + NaCl 0.5M solution or distilled water were strongly affected by corrosion.
4. The frequency band of the elastic wave was divided into dominant frequency below about 50 kHz and above about 60 kHz, regardless of the value of Kc. The low-frequency band below about 50 kHz is the elastic wave due to corrosion, while the high-frequency band above about 60 kHz is the elastic wave caused by crack occurrence and propagation.
5. When K_C was the smallest, the crack in the surface direction propagated slightly, but the crack in the depth direction did not propagate at all. The stress intensity factor at this time was determined as the HAC threshold stress intensity factor (K_{IHAC}). That is, K_{IHAC} was determined to be 1.96 MPa$\sqrt{m}$.
6. The static fatigue limit was determined to be 400 MPa, and the static fatigue limit of the crack specimen can be evaluated using $K_{IHAC(a)}$ = 1.96 MPa $\sqrt{m}$). The experimental results agreed well with the evaluation results.

The frequency characteristics of elastic wave will be provided the basic data for monitoring crack initiation and propagation in UHSS structural components that have been exposed to various harsh environments. These results will provide basic data for monitoring structures in which HAC occurs, and for predicting the HAC behavior of UHSS. HAC can be prevented by minimizing contact between the high-strength metal and hydrogen. However, when HAC occurs, it can be monitored through elastic wave detection. These results can be used as data to evaluate the fatigue limit of UHSS under a corrosive environment and to secure the stability of chemical plants.

Publication paper of Journal

1. Ki-Woo Nam, Ki-Sik Lee, Kong-Young Kim (2020.08), “Elastic Wave Characteristics of STS316L with Degree of Different Cold Rolling”, Journal of Power System Engineering Vol. 24, No. 4, pp. 11-16.
2. Ki-Woo Nam, Ki-Sik Lee, Young-Joon Tak and Gong-Young Kim (2020.10), “Elastic Wave Properties of STS316L according to Thickness and Welding Method by Hsu-Nielsen Source”, Journal of Power System Engineering, Vol. 24, No. 5, pp. 5-11.
3. Hak-Chul Kim, Ki-Sik Lee, Young-Joon Tak, Ki-Woo Nam, Byoung-Chul Choi (2021.02), “Effect of Forming Method on Tensile Properties of Elbow”, Journal of Power System Engineering, Vol. 25, No. 1, pp. 36-42.
4. Young-Joon Tak, Ki-Sik Lee and Ki-Woo Nam (2021.06), ”Mechanical Properties of Nitrogen Bubbled SD500 Rolled Steel“, Journal of Power System Engineering, Vol. 25, No. 3, pp. 30-37.
5. Ki-Woo Nam, Hyun Jeon, Ki-Sik Lee and Young-Joon Tak (2021.06), ”Elastic Wave Properties of STS202 depending on Rolling Temperature and Rolling Degree“, Journal of Power System Engineering, Vol. 25, No. 3, pp. 15-22.
6. Ki-Sik Lee, Jae-Eun Paeng, Kyoung-Hee Gu, Ki-Woo Nam (2021.06), “Threshold stress intensity factor of ultra-high strength steel (HV670) containing surface crack by hydrogen assisted cracking and cumulative elastic wave”, Journal of Mechanical Science and Technology, Vol. 35, No. 6, pp. 2441–2447.
7. Kyoung-Hee Gu, Ki-Sik Lee, Gum-Hwa Lee, Ki-Woo Nam (2022.06), Evaluation of Fatigue Life of Ultra High Strength Steel under Stress Corrosion Environment, Applied Mechanics and Materials, vol. 907, pp. 1-7.
8. Gum-Hwa Lee, Ki-Sik Lee, Ki-Woo Nam, Elastic Wave Properties in Ultra-High Strength Steel (HV670) exposed to Various Corrosive Solutions”, Journal of Mechanical Science and Technology (투고중)

Paper of proceeding

9. Byeong-Su Kim, Jae-Eun Paeng, Ki-Sik Lee, Ki-Woo Nam, “Characteristics of Elastic Wave of SKD11(HV670) by Hydrogen Assisted Cracking”, Proceeding of The KSME 2019 Annual Meeting, pp. 1813-1816.

10. Ki-Sik Lee, Young-Joon Tak, Jae-Eun Paeng, Min-Heon Kim, Cheol-Su Kim and Ki-Woo Nam, 2020, “Static Fatigue Life of SKD11 under Corrosion Environment”, Proceeding of The Korean Society for Power System Engineering 2020 Fall Annual Meeting, pp. 1-3.
11. Hyun Jeon, Ki-Sik Lee, Young-Joon Tak, Kyoung-Hee Gu and Ki-Woo Nam, 2020, “Mechanical Properties of STS202 according to Rolling Degree”, Proceeding of The Korean Society for Power System Engineering 2020 Fall Annual Meeting, pp. 7-9.
12. Young-Joon Tak, Ki-Sik Lee, Jae-Eun Paeng, Min-Heon Kim, Kyoung-Hee Gu and Ki-Woo Nam, 2020, “Weibull Probability Distribution for Vickers Hardness of SD500 Steel with N2 Bubble”, Proceeding of The Korean Society for Power System Engineering 2020 Fall Annual Meeting, pp. 12-13.
13. Kyoung-Hee Gu, Ki-Sik Lee, Seok-Hee Kang, Chang-Yong Kang, Sang-Hyun Park, Ki-Woo Nam, 2021, ”Stress Corrosion Static Fatigue Limit of HV670 Steel“, Proceeding of The KSME 2021 Annual Meeting, KSME, pp. 1226-1228.
14. Kyoung-Hee Gu, Gum-Hwa Lee, Ki-Sik Lee, Ki-Woo Nam, 2022, „Evaluation of Static Fatigue Limit of SKD11 Under Stress Corrosion Environment”, Proceeding of The Korean Society for Power System Engineering 2022 Spring Annual Meeting, pp. 139-140.

Acknowledgement

My deepest gratitude goes first and foremost to Professor Ki-Woo Nam my supervisor, for his constant encouragement and guidance. He has led me through all the stages of the writing of this article. Without his consistent and instructive guidance, this thesis is unlikely to reach its current form. Thank you so much, you are such an excellent academic advisor. Thank you again for giving me the opportunity.

In addition, I am especially grateful to the members of the thesis review committee: Professor Byung-Gun Ahn, Dr. Heoung-Joo Kang, Dr. Kong-Young Kim, Dr, Jae-Yong Hyun, Professor Hyungseok Nam. I am also deeply grateful to all other tutors and professors for their direct and indirect help.

My parents and my wife (Ji-Yun Won), of course, thanks for support and everything. My brothers, sisters and my sons (Hyung-Jun and Hyung-Gug), love all of you. I also owe my sincere gratitude to my friends and my colleague who gave me their help and time in listening to me and helping me solve my problems during the difficult course of the thesis.

December 20, 2022
Lee, Ki-Sik